Universidad de los Andes

Physics department

Measurement and Characterization of Granulation Pattern in the IAG Solar Flux Spectrum

First version

BSc Physics Final Project

Author:

Claudia Alejandra Cuellar Nieto

Advisor:

Benjamin Oostra Vannoppen

Nov 2025

Abstract

Hello, this is my work:D

Acknowledgements

Contents

List of Figures

3

Chapter 1

Introduction: The Sun's granulation pattern

For decades, the solar spectrum has served as the fundamental reference point for spectroscopic analysis. As our nearest star, the Sun enables detailed studies of stellar composition. However, advances in optical instrumentation have revealed previously undetected spectral details, providing new insights into fundamental solar properties One key insight is the granulation pattern caused by convective motion, which is characterized by three distinct hydrodynamic signatures: Line broadening, line bisector asymmetry, and the line-depth dependence of convective blueshift.

Inspired by David Gray's foundational research ([8] and references therein), this project aims to extract the granulation pattern from the IAG Solar Flux Atlas to calculate relative velocities and perform a detailed analysis based on the three signatures of convection.

1.1   Convective motion

The stellar spectrum serves as astronomy's primary source of information, encoding details about a star's composition and velocity. However, in some stars this spectrum is modified by fluid motions caused by density variations from temperature fluctuations in the outermost layer, where each spectral line exhibit a distinct velocity shift. These persistent convective

motions generate a granular structure in the solar photosphere, a phenomenon supported by extensive research (see [9, 10, 8]).

The granulation was first observed as a granular structure in movement by Janssen in 1885. Later, in 1901, Plaskett associated this pattern with the convective cells observed in Bénard's experiment [4], where fluids heated from below produces rising elements of hot gas convecting heat to the surface. This characteristic configuration gives the name *granulation* to all observable signs of solar convection.

1.1.1 The three signatures of convection

Convective motion produces three distinct signatures of granulation in stellar spectra: Line broadening, line bisector asymmetry, and line-depth dependence of convective blueshift [11]. This project focuses on the third signature, which exhibits a correlation between line depth and relative velocity. The method for quantifying this relationship is known as the *granulation pattern*, which means the plot of relative velocities against line depth [8].

The physical origin of this pattern lies in the convective process itself. When the Sun pushes material up through its outer layer, the spectrum exhibits a blueshift. As this material subsequently cools and falls back through the atmosphere, it produces a redshift but emits less light, making the blueshift dominant. Neutral iron lines (Fe I) are optimal for calibrating this phenomenon due to their high abundance, minimal thermal broadening, and limited isotopic variation. This approach offers the additional advantage of deriving natural wavelengths from a single source, thereby eliminating potential discrepancies.

The study of granulation patterns has been significantly documented by David Gray, whose work has improved the precision of stellar radial velocity measurements ([8] and references therein). This improvement stems primarily from his observation that granulation patterns in solar-type stars closely resemble the solar pattern, differing primarily by a scaling factor. This is particularly significant given the considerable challenges of obtaining such precise measurements for other stars, which are often affected by spectral noise, stellar proper motions, and velocity uncertainties [8]. Furthermore, analyzing solar granulation patterns is crucial for validating photospheric hydrodynamic models [10], enabling improved calibration and testing

of dynamic atmospheric models.

Following the motivation of treating the Sun as any other star, which does not have the proximity for spectra study, the most accurate solar flux atlas is necessary.

1.2   IAG Solar Flux Atlas

In 2016, Reiners and colaborators published the unprecedented precision *Institut für Astrophysik Göttingen (IAG)* Solar Flux Atlas obtained with the FTS *Fourier Transform Spectrograph* at Göttingen, simultaneously reporting convective blueshifts for a sample of Fe I lines. This atlas provides highly precise and accurate data, with radial velocity uncertainties on the order of $\pm 10 m/s$ across the wavelength range of 4050 to 10650 $\mathring{A}$. In contrast to other FTS atlases, the entire visible wavelength range was observed simultaneously using only one spectrograph setting [12].

Despite the exceptional quality of the spectrum, the first derived granulation pattern appeared notably scattered and noisy. This was attributable to a rudimentary line position measurement methodology and a poorly line selection, which included numerous blended features, outdated wavelength references, and incomplete spectral coverage. Consequently, the full potential of the IAG atlas for determining precise convective blueshifts remains unrealized, highlighting the need for the refined analytical methods applied in this project.

1.3   IAG Spatially Resolved Quiet Sun Atlas

In 2023, Ellwarth and colaborators [6] published the *Institut für Astrophysik Göttingen (IAG)* Spatially Resolved Quiet Sun Atlas, also obtained with the FTS *Fourier Transform Spectrograph* at Göttingen. This atlas has the advantage of its coverage from the disc center ($\mu = 1.0$) towards the solar limb ($\mu = 0$), where $\mu = \cos(\theta)$. This spatial resolution enables the study of how convective blueshifts vary across the solar disc due to changing projection angles, a dependency that cannot be observed in other stars.

The principal objective of this project is to characterize the solar granulation pattern by treating

the Sun as any other star. To achieve this, the disk-integrated IAG Solar Flux Atlas serves as our primary data source. However, a precise analysis of the relative velocities in this integrated light requires correcting for the center-to-limb variations that are uniquely quantified by the Spatially Resolved Quiet Sun Atlas.

1.4 Motivation

In the first semester of 2025, Manuel Fuentes a physics student at the Universidad de los Andes, implemented these improvements in a computational project focused on the visible spectral range. By developing enhanced measurement techniques and employing a carefully curated line list that fully covers the visible range with updated wavelength references, Fuentes achieved significantly sharper granulation patterns than previous analyses. This work demonstrated that proper line selection and modern wavelength standards can reliably extract convective signatures from high-quality solar spectra.

Under the guidance of Professor Benjamin, this project extends the analysis into the near infrared range. This region contains spectral lines that originate from deeper photospheric layers. Although these lines are consequently weaker, they represent a rich source of information. However their analysis requires an adaptation of the existing measurement methodology. A key objective was to adapt these methods to enable the characterization of solar dynamics and line asymmetries via granulation patterns in the near infrared range.

By addressing these challenges, this project aims to produce a robust characterization of the solar granulation pattern and new insights into the photosphere's dynamic. These efforts are guided by the central research question: What are the direct spectroscopic consequences of solar dynamics?

Chapter 2

Literature Review: Convective motion in the Sun

As previously mentioned, David Gray has significantly advanced the study of granulation patterns in the solar photosphere, with a particular focus on measuring relative velocities with high precision. This chapter explores the three signatures of convective motion in the Sun photosphere, and how this reveals the hydrodynamics on this outermost layer.

2.1 The solar interior and the solar outer atmosphere

The Sun is classified as a yellow dwarf star of spectral type G2V. Its chemical structure is primarily composed of a large fraction of ionized hydrogen and a smaller proportion of helium. What makes the Sun unique in astronomical studies is its proximity to Earth, which allows for detailed observation unmatched for any other star. Structurally, the Sun is divided into two main regions: The solar interior and the solar outer atmosphere.
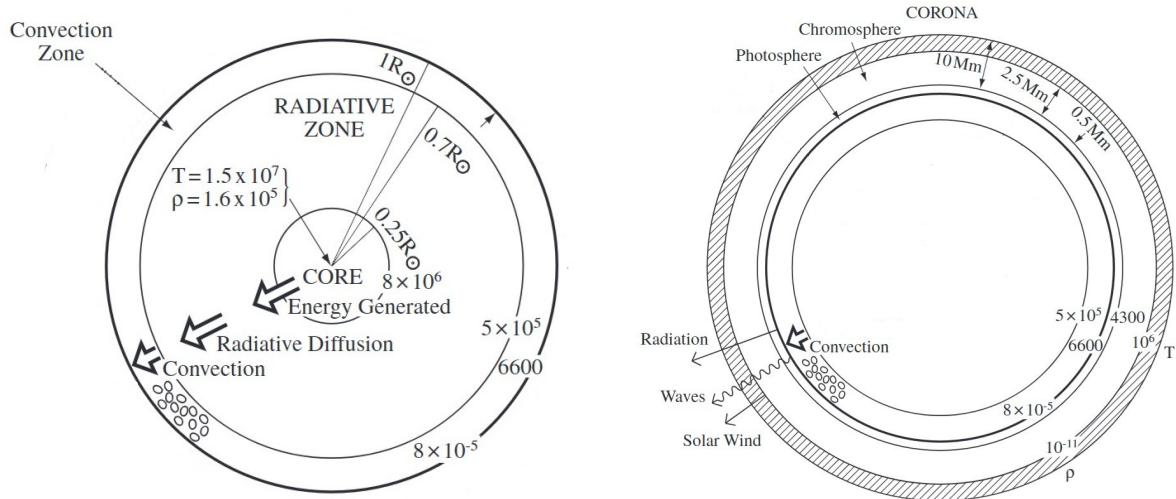
(a) The interior structure of the Sun. The convection zone is responsible for the general movement that characterizes the third signature.

(b) The outer structure of the Sun. The photosphere is the layer of the sun where the convection cells overshoot from the convection zone.

Figure 2.1: The general structure of the Sun. Image modified from [1].

As illustrated in the Figure 2.1a the overall structure of the solar interior is core, radiative and convective zone. Moving outward through these layers, both the density and temperature decrease significantly, as the energy is slowly transferred outwards by radiative diffusion. In the core, where energy is generated by thermonuclear fusion, standard models estimate a temperature of $1.6 \times 10^7 K$ and density to $1.6 \times 10^5 Kg/m^3$. The extreme conditions in this region maintain the central material in a plasma state, functioning like a massive nuclear reactor. This characteristic high density allows the absorptions and remissions of photons that make this zone highly opaque. This process, known as radiative diffusion, slowly transfers energy outward and progressively shifts the wavelength of the radiation from high-energy $\gamma-$rays to the visible light that eventually escapes.

On the other hand, the Figure 2.1b illustrates the overall structure of the solar outer atmosphere which consists of the photosphere, chromosphere and corona. In these layers, the density decreases rapidly with height above the solar surface. The temperature decreases to a minimum of approximately $4300 K$ in the upper photosphere before rising through the chromosphere and transition region to millions of degrees in the corona. Thereafter, the temperature falls slowly

11

expanding outwards as the solar wind.

The most relevant layer for this project is the photosphere. This thin layer of plasma that emits most of the solar radiation and a continuous spectrum. When this continuous light passes through the overlying chromosphere, specific wavelengths are absorbed, resulting in the characteristic Fraunhofer lines superimposed on the continuum [1].

The target layers of this study are the convection zone and the photosphere, which will focus in further sections.
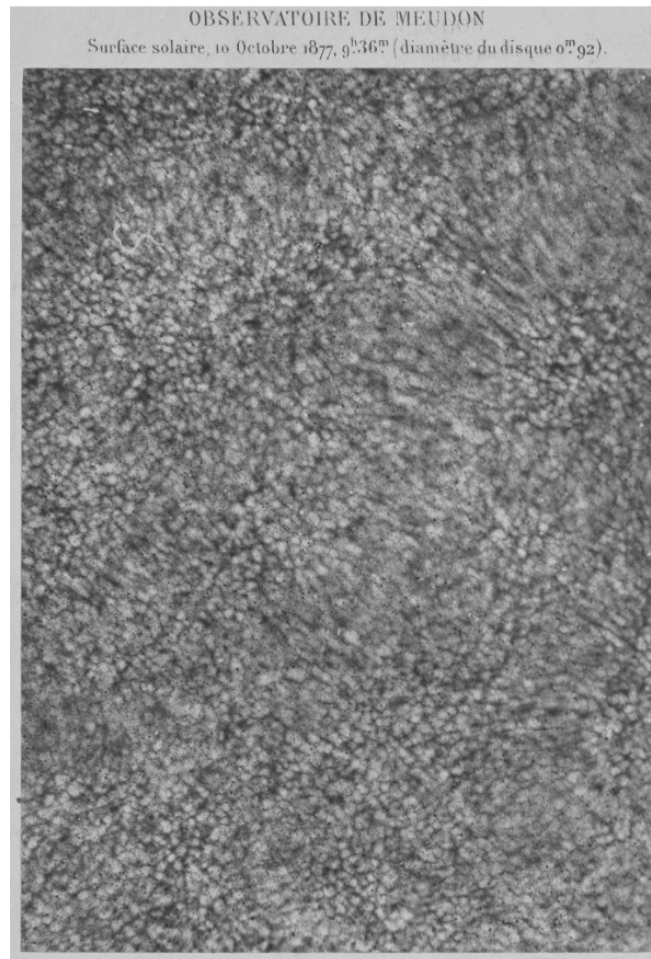
Figure 2.2: The first clear photograph of the photosphere where the granulation pattern is visible. Image taken from [2]

In 1885 Janssen obtained the first clear photograph of photospheric granules [2] providing the initial evidence for this granularar pattern (see figure 2.2) This was the starting point for dif-

ferent studies across the pattern of these granules. In 1930, Unsöld theorized that the layers beneath the photosphere should be convective unstable [4]. This hypothesis was later supported when Plaskett related the observed granules to the convective cells studied in Bénard's laboratory experiments [13]. In this analogy, a fluid heated from below develops rising elements of hot gas that transport heat to the surface.

These convective elements are known as granulation, with each individual region referred to as a granule. Typical granules span approximately 700 km and have short lifetimes, lasting between five to ten minutes. The understanding of granules as convective cells provided direct evidence for the existence of a zone responsible for convective motion beneath the photosphere.

2.2 The solar convection Zone

The convective zone, where dynamic plasma motions occur, begins at approximately $0.86R_\odot$. The great temperature gradient across this layer allows the convective process [1].

2.2.1 The convection movement in the sun

As previously mentioned, convection is driven by fluids heated from below representing hot rising gas elements or *convective cells* transporting heat to the photosphere [13]. In the solar context, convection takes place in a highly compressible and stratified gas. This physical regime leads to determine the conditions required for convection to occur and the resulting dynamics of the granules [4].

2.2.2 Dynamics of solar convection

From the core, He nuclei is built from H nuclei in the proton-proton chain as equation (2.1) refers.

$$4^1H \rightarrow^4 He + 2e^+ + 2\nu + 26.7 MeV \tag{2.1}$$

The proton-proton chain reaction in the core liberates a considerable amount of energy in the

form of high-frequency γ-rays (approximately 26.7 MeV) and neutrinos (0.5 MeV). However, the strong Coulomb repulsion between positively charged nuclei, which increases with the product of their nuclear charges, means that only the lightest elements have appreciable fusion probabilities.

As energy is transported outward, photons are frequently absorbed and re-emitted. This process reduces the radiative conductivity, which in turn increases the temperature gradient [4]. When the transported energy reaches the low photosphere, a portion of the radiation escapes into space, and the plasma returns to a state of convective stability [1]. These conditions establish the onset of convection.

Consider a granule of plasma in local hydrostatic equilibrium with its surroundings, characterized by radial profiles of pressure $P(r)$, density $\rho(r)$, and temperature $T(r)$. If the granule's temperature is increased to a value T', it will expand adiabatically to maintain pressure equilibrium, thereby decreasing its density relative to its surroundings.

This lower-density gas then experiences a buoyancy force, causing it to rise. The buoyancy force persists until the granule's density matches that of its new surroundings after traveling a mixing length l. Let T'_n be the temperature of the rising element and T_n the temperature of its new surroundings. The difference between the adiabatic gradient of the element and the radiative gradient of the surroundings governs the convection, as described by the equation (2.2)

$$T_n = T + \left(\frac{dT}{dr}\right)_R l \quad \Big| \quad T'_n = T' + \left(\frac{dT}{dr}\right)_{ad} l \tag{2.2}$$

Where R refers for radiative temperature gradient and ad for the adiabatic temperature gradient. Convection occurs when the radiative gradient becomes steeper than the adiabatic gradient. Since we have assumed radiative equilibrium, the R denotes the gradient present in the stellar atmosphere.

The onset of convection leads to the inequality (2.3), where two conditions can arise: The convection pattern is established when radiative gradient exceeds the adiabatic gradient; otherwise, the layer is stable and energy is transported by radiation.

$$-\left(\frac{dT}{dr}\right)_R > \left(\frac{dT}{dr}\right)_{ad} \tag{2.3}$$

14

If the convective pattern is established, the element continues to expand adiabatically as it rises, driven by buoyancy. Otherwise, if the layer is stable, the element will contract, becomes heavier than its surroundings and begins to move down toward its original position.

This onset of instability, when the vertical temperature gradient is too large, is formally described by the Schwarzschild criterion for convection.

2.2.3 The Schwarzschild criterion

Taking the element described before, now suppose an elementary parcel of material displaced so slowly that remains in horizontal pressure equilibrium (see figure 2.3).
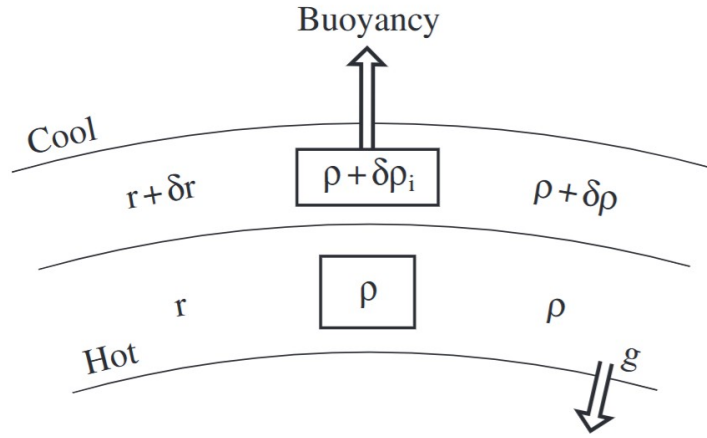
Figure 2.3: Diagram for the parcel of material displaced so slowly that remains in horizontal pressure. Image taken from [1]

If the motion is adiabatic there is no heat exchange with surroundings, the pressure and density of the rising element are adiabatic. This generates a criterion for the presence of convection known as the Schwarzchild criterion (2.4).

$$-\frac{dT}{dr} > \frac{\gamma - 1}{\gamma} \left(\frac{GM_\odot m}{r^2 k_B} \right) \tag{2.4}$$

Where k_B refers to Boltzmann constant; G the gravitational constant; $M_\odot$ the solar mass; m the mass of the granule; and γ the adiabatic index. The presence of convection reduces the temperature gradient from the higher value required for purely radiative transport to a adiabatic

15

value [4]. The material and energy transported by this process ended up to low photosphere, where the granules exhibit different properties that will be examined in subsequent sections.

2.3   The Solar Photosphere

Since 1874, when Langley gave a detailed description of granulation on the photosphere, astronomers have studied the dynamics and reactions within Sun's outermost layer [1]. A distinct pattern of granules with dynamic behavior is apparent, where individual cells continuously emerge and disappear (see Figure 2.4).
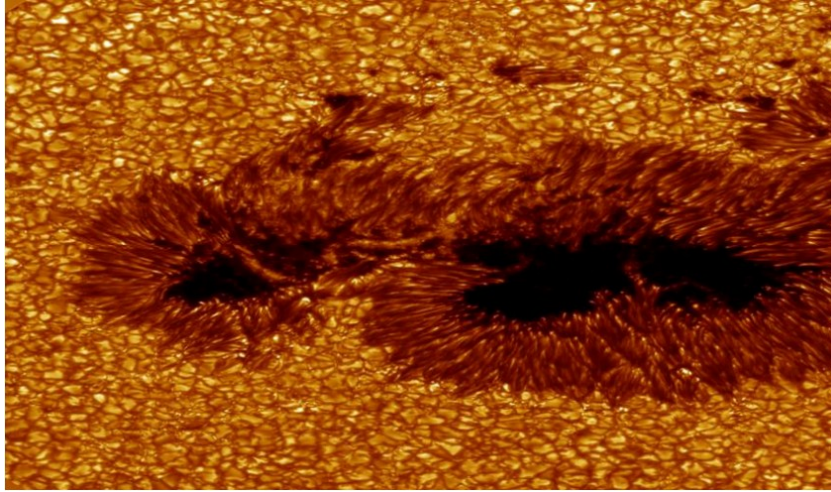
Figure 2.4: A view of granulation on the Sun's surface. The central regions exhibit blueshifts while the edges display redshifts. Image taken from [3]

The bright areas of granules correspond to regions where hot gas rises through the solar atmosphere. As this gas releases energy in the form of photons at the photosphere, it cools and subsequently descends, creating the darker regions of granules [14].

2.3.1   Static photosphere: Limb darkening phenomenon

Because the temperature decreases outward through the photospheric layers, the observed intensity falls off towards the solar limb. This effect is known as *Limb darkening phenomenon*,

discovered by Halm in 1907 [10]also causes the disk intensity profile to appear more squared at increasing wavelength (see Figure 2.5).
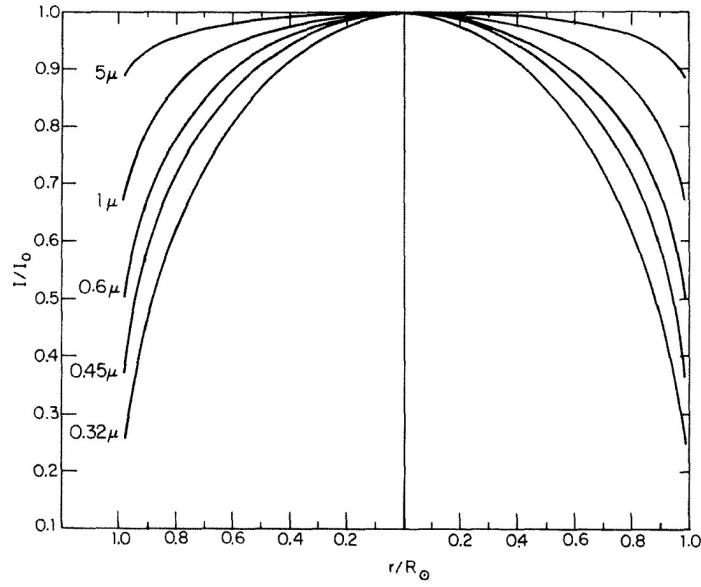
Figure 2.5: Squared profile for the disk intensity at increasing wavelengths. Image taken from [4]

The analysis of this effect provides a direct technique for determining the temperature structure of the photosphere as a function of depth.

Furthermore, high-resolution observations reveal that these granules has shown to be in continual motion (see Figure 2.6).

17
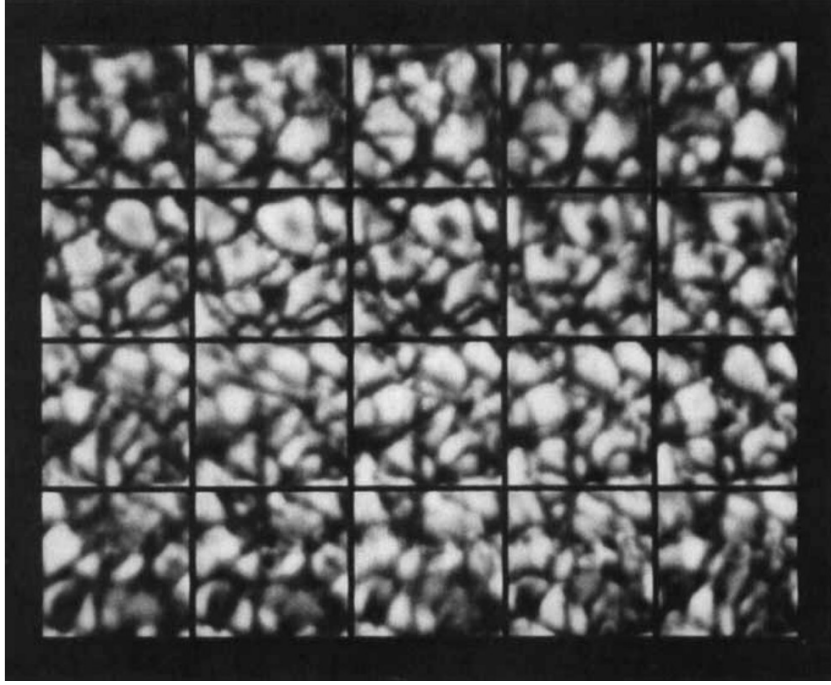
Figure 2.6: A time sequence showing granule evolution where the time intervals are about a minute. Image taken from [4]

This perpetual motion across the photosphere generates asymmetries in absorption line profiles. For typical weaker lines, the convective blueshift diminishes toward the limb, with a net velocity change approximately of $400 m/s$. As explain Ellwarth et al. observations closer to the limb pass through the atmosphere a shallower angle. This results in longer optical paths through high atmospheric layers, allowing the gravitational redshift to dominate the measured signal [6].

2.3.2 Dynamic photosphere: The C-curved profile bisector.

Analysis of granule dynamics reveals a height dependence of convective velocities: The vertical velocity of a rising granule decays less rapidly than its excess brightness. Changes in the granulation structure, contrast and velocity field around the spots and magnetic network have been inferred indirectly from observations of Fraunhofer line profile shapes [4]. A direct result of the correlation between brightness and velocity of granules is the characteristic C-curved line profile bisector observed in photospheric absorption lines (see figure 2.7).

18
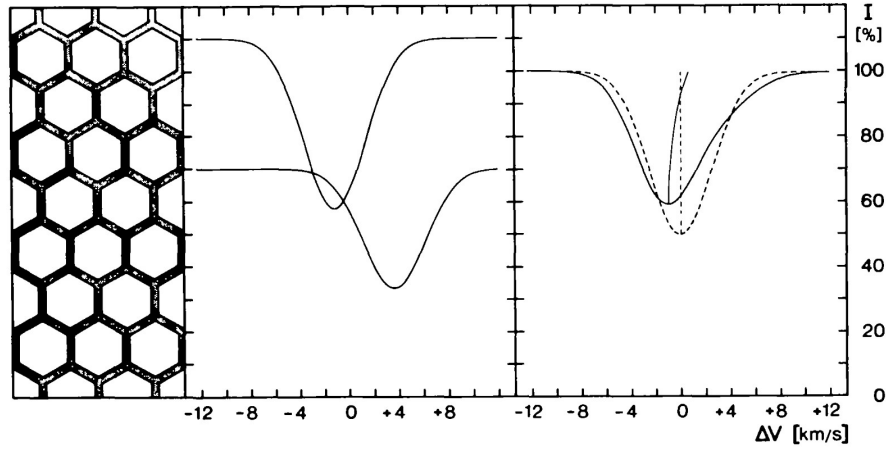
Figure 2.7: The C-curved line profile bisector. In the infrared shown to be less pronounced than violet range.

The formation of the C-curved line profile bisector occurs in three stages, corresponding to different heights in the photosphere.

First, the mid-depth portion of the line profile is formed in the brightest upflowing material, resulting in a blueshift. Then, the deepest part of the line core is formed higher up, in a region of decelerated upflow, producing a smaller blueshift. Finally, the line wings where the opacity is lowest, tend to be formed deepest in the cool material, resulting in a redshift.

This dynamic process induces characteristic perturbations in spectral lines, manifesting as line broadenings, line profile asymmetries, and line depth-dependent wavelength shifts known as the three signatures of convection [11].

2.4   The three signature of convection

The signatures of convection in stars are described by Gray in his research [8, 7, 11] as the principal characteristics to identify and treat the asymmetries due to convective motion.

2.4.1   First signature of convection: Line broadening

Due to the limb darkening phenomenon and atmospheric absorption, there exists two types of line cores: Strongest and weaker lines [11]. In general, stronger absorption lines exhibit more
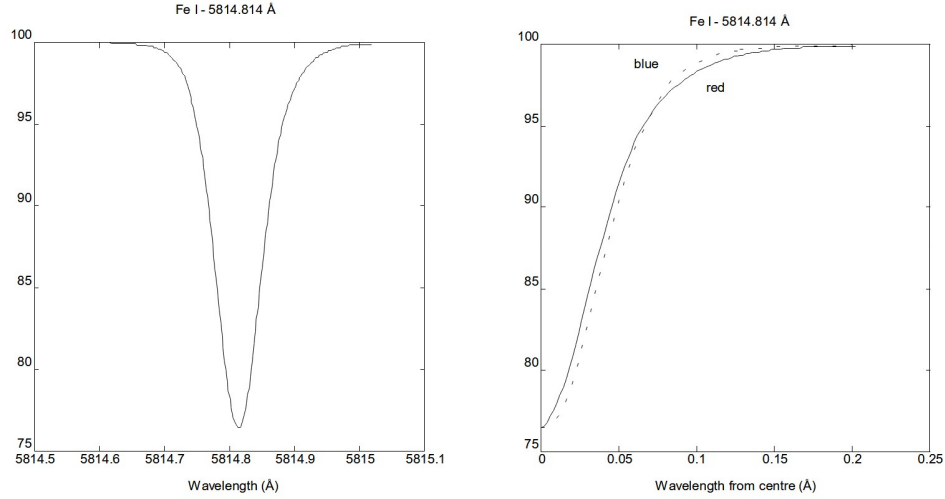
Figure 2.8: Asymmetries on an average absorption line. Can be observed the differences in intensity redshift profile. Image taken from [5]

pronounced core curvature than weaker lines. This line core curvature C_c can be quantified by the second derivative of the line's intensity profile with respect to wavelength, evaluated at observed wavelength (see equation (2.5)).

$$C_c = \lambda_{obs}^2 \left(\frac{d^2 p(\lambda_{obs})}{d\lambda_{obs}^2} \right) \tag{2.5}$$

In the near infrared range, the solar spectrum contains natural bands or groups of lines that are separated by regions of strong absorption from telluric elements. In other words, elements like O_2 and CO_2 that are absorbed by the atmosphere. This phenomenon can altered the line core curvature of determining lines profiles, specially in the near infrared range.

2.4.2 Second signature of convection: Line profile bisector asymmetry

As demonstrated by Nieminen [5], the asymmetry occurs because the c-curved profile bisector reflects velocity variations and a bisector slope (see figure 2.8).

According to Kirchhoff's laws, absorption line formation requires lower temperature conditions, which are found precisely in the Sun's outermost atmospheric layers [14]. These regions not only provide the appropriate temperatures for absorption but also exhibit comparatively

higher opacity. Among all available spectral lines, those from Fe I are particularly valuable for solar granulation studies due to two key characteristics: They display significant opacity and relatively low thermal broadening. These properties make Fe I lines excellent tracers of granulation patterns in the solar photosphere [5].

These asymmetries imprinted on these Fe I lines can be quantified by analyzing their bisectors. A powerful method for this involves using the third derivative of the line profile, which provides a measure of the bisector's shape and curvature (see Equation (2.6)).

$$\frac{c}{\lambda_{obs}} \left(\frac{1}{3C_c^2} \right) \left(\frac{d^3 p(\lambda_{obs})}{d\lambda_{obs}^3} \right) \tag{2.6}$$

Since most of stellar observations are made with lower-resolution spectrographs and often lower signal-to-noise ratios, there is a need to study granulation through its signatures. Gray and Oostra identified a form of line profile asymmetry observable under these conditions, known as the *flux deficit*. This phenomenon can be interpreted as flux imbalances on the red-shifted side of the line profile, caused by a net loss of radiative energy. Consequently, the line's bisector becomes inclined relative to its original, symmetric position.

To quantify this asymmetry, the authors proposed calculating the flux deficit by taking the difference between the observed, altered profile and a reference symmetric profile. By treating the altered line profile as an approximate representation of the third signature of convection, one can observe the flux difference interpreted as radiation [7].

2.4.3 Third signature of convection: Line depth-dependent wavelength shifts

Many studies across the years have detected and observed the phenomena of wavelength shifts against the line depth, or as it is called, chromodependence in the granulation pattern. This behavior was shown to be more present in the weaker lines which are related to infrared and violet range.
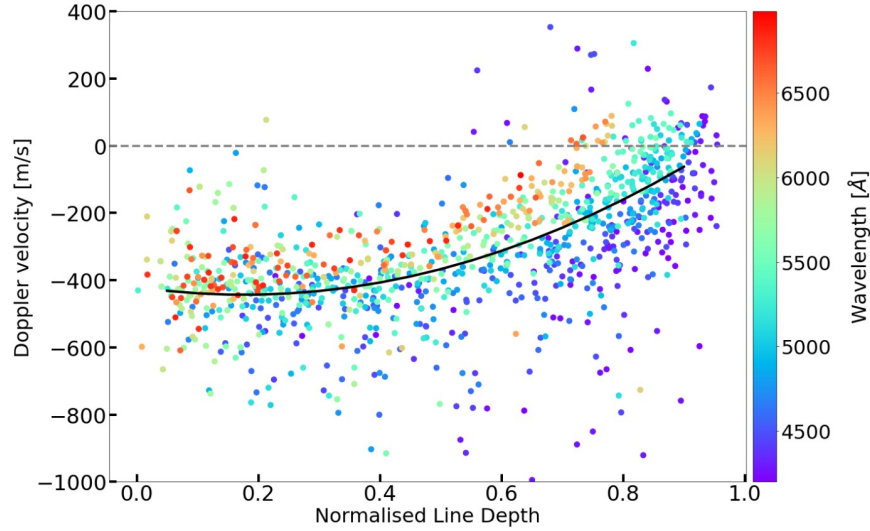
Figure 2.9: Granulation pattern for the IAG spatially resolved quiet sun atlas, is shown to have a strong chromodependence in the weaker lines. Image taken from [6].

2.4.4 Solar granulation pattern

The solar granulation pattern is a plot of relative velocity against line depth, as shown in the Figure 2.9.

he significance of the granulation pattern lies in its universality for solar-type stars; their patterns closely resemble the Sun's, differing primarily by a scaling factor (see [11]). Consequently, a detailed analysis contributes to the understanding and radiation of photospheric hydrodynamic models [10, 8]. However, a precise measurement of the granulation pattern requires a understanding of the convective blueshift phenomenon.

Convective Blueshift

When the Sun pushes material up through its outer layer, the spectrum exhibits a blueshift. As this material subsequently cools and falls back through the atmosphere, it produces a redshift, but emits less light, making the blueshift dominant. That can be measure by the Doppler effect but as the velocities can be significant, the relativistic formulation of this effect must be applied.

The relativistic Doppler effect accounts for length contraction, as predicted by Einstein's theory

of relativity. This introduces an additional correction term to the classical shift, which becomes particularly relevant in high-velocity scenarios or strong gravitational fields. However, the measured negative redshift resulting from convective motions is known as *convective blueshifts* which are measured by the equation (2.7).

$$v_r \approx c \left(\frac{\lambda_{obs} - \lambda_{rep}}{\lambda_{rep}} \right) \tag{2.7}$$

Since the strength of the convective distortions and shifts as spectral lines vary across the H-R diagram, we expect systematic errors in radial velocities [8].

2.4.5 Chromodependence characterization

Recent emphasis on measuring the granulation pattern has led to new interpretations of line depth-dependent wavelength shifts. However, a comprehensive characterization of this phenomenon is still missing.

In 2018, Gray and Oostra attempted to establish a standard curve determined by a third order polynomial fit to the solar granulation pattern (see figure 2.10).
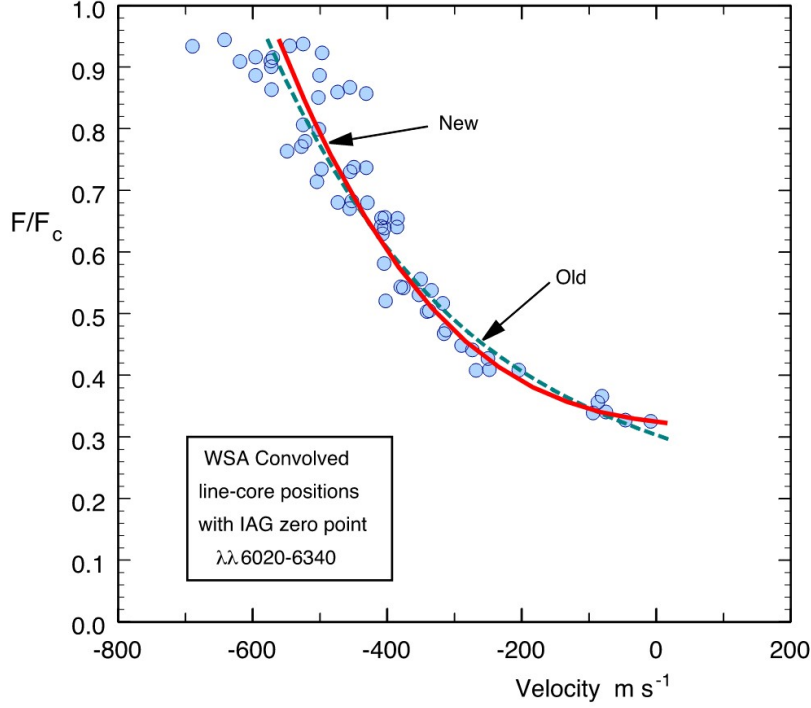
Figure 2.10: Standard curve proposed by Gray and Oostra on the spectral range the spectral range of $4950\mathring{A}$ to $5700\mathring{A}$. Image taken from [7].

Nevertheless, the authors limited the spectral range of $4950\mathring{A}$ to $5700\mathring{A}$, thereby avoiding the chromodependence in weaker lines. This limitation motivates the present work to develop a strong characterization and give the methodology for dealing with this phenomenon.

A separate theoretical perspective, offered by Hamilton and Lester, attributes aspects of photospheric dynamics to rotation. The pronounced differential rotation with latitude observed seems to be the result of convective flows driven radially by the buoyancy force and deflected horizontally by the Coriolis force [4]. This rotation contributes to angular momentum through two forms: Meridional circulation and Reynolds stresses.

The first contribution involves axisymmetric meridional circulation (see Figure 2.11). In the absence of other transport mechanism, such a circulation would tend to spin up the poles and the interior, as the moving fluid conserves its angular momentum.

The second contribution, which tends to enforce solid body rotation, arises from Reynolds stresses associated with nonaxisymmetric convective motions. The mechanism can be un-

24

MERIDIAN CIRCULATION

REYNOLDS STRESSES
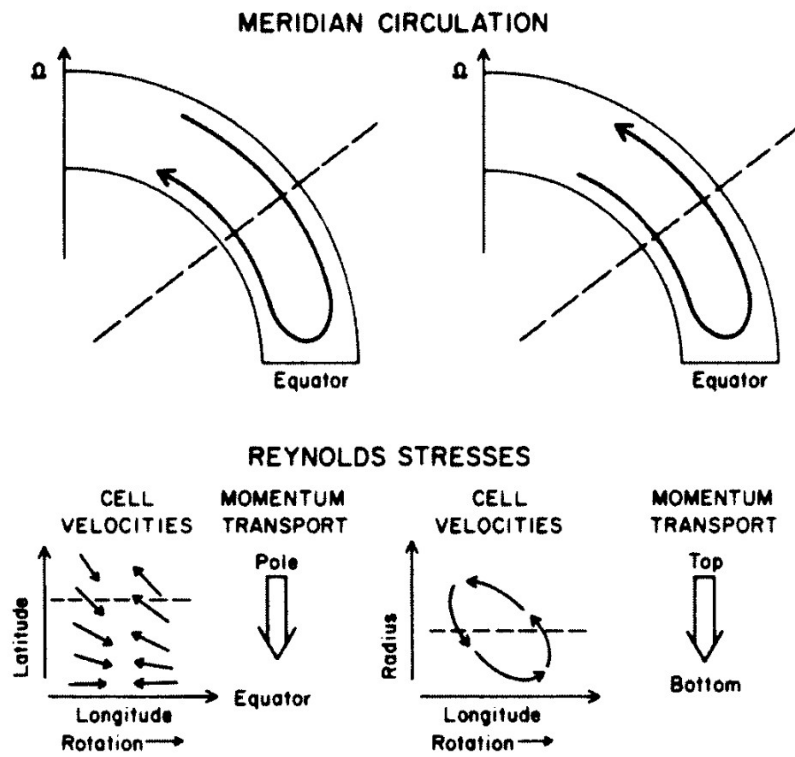
Figure 2.11: Contributions on angular momentum. Image taken from [4].

derstood by considering that, for equal velocities in the meridional plane, the flux of angular momentum per unit mass is greater toward the equator than away from it. This process depends critically on nonaxisymmetric convection, as it generates net fluxes of angular momentum in latitudinal and radial directions without a corresponding net mass flux. Neither buoyancy forces, which are strictly radial, nor pressure gradients, which must average to zero around the solar circumference, can directly influence the sun's axisymmetric rotation profile [4]. Therefore, the combined action of meridional circulation and Reynolds stresses is essential for shaping the observed differential rotation.

Chapter 3

Methodology: The blend-free list of Fe I lines

As the spectral analysis is complicated due to convective motion this project takes a computational approach leading to an observational requirement, by the experience of professor Benjamin and previous research. For the computational part, the programming language Python was used. All analysis data and code used in the process was uploaded to a GitHub repository, allowing anyone interested to reproduce the results and verify the authenticity of the conclusions presented.

We follow the methodology established in previous studies (see [10] and references therein), which utilized a selected list of Fe I lines. As mentioned before these lines are ideal for this calibration due to their minimal thermal broadening and reduced susceptibility to other atmospheric affectations.

3.1 Computational approach

The computational aspect focuses on identifying the granulation pattern within the solar spectrum by calculating relative velocities using the wavelengths of Fe I.

The line up was to identify the Fe I lines in the IAG Solar Flux Atlas and the IAG Spatially Resolved Quiet Sun Atlas using the blend-free list of Fe I lines. Second, bins of $0.05m\mathring{A}$ were

selected around the closest minimal point to each line from the Fe I list. With this, a fourth-grade polynomial fit was fitted due to the c-curved line profile bisector and found the observed wavelength. Allende and Garcia showed the accuracy of using a fourth-order polynomial fit and only taking the slope for the bisector to know a measure of asymmetry [**?**]. For an optimal fit was used a z-score standardization on each line core, which is explained in appendix A. Then the observed wavelength, relative velocity and convective blueshift were calculated based on the polynomial fit. Finally, the values for the line core curvature (see equation (**??**)) and the line core bisector slope (see equation (**??**)) were found.

3.2   Blend-free Nave Fe I line list

The previous line up implemented the Nave list of laboratory measured Fe I lines [15]. This list classifies lines with a quality rating (A,B,C,D) with A be the most and best quality. However, not all the listed lines are clearly present in the solar spectrum, and within the near-infrared range, many lines are severely mixed.

In collaboration with Professor Benjamin and Manuel Fuentes, we refined this list using different approaches.

3.2.1   Selection process for blend-free Fe I lines

The process of selection has two different approaches: Computational and visual. First, we selected only quality A lines for the Nave list and then performed 4 filters according to the statement of having a fourth order polynomial fit for the line core.

The first filter is taking into account the form of the C-curved line profile bisector. If the bisector presents a majority of scattered points, the line core is affected by the noise.

The second filter consists of selected lines whose curvature sign obeys an absorption line. In other words, the coefficient of the fourth grade term needs to be positive. A filter on the magnitude of these coefficients was discarded because the weaker lines, that are essential to see, have a small curvature. Furthermore, lines in the near infrared range have big core curvatures related to atmospheric lines.

The third filter consists of taking lines which represent a curve, discarding closest points which don't represent a Fe I line on the solar spectrum. In other words, take lines which are seen as slopes or don't have a core. For this, the difference between extreme points of the fit needs to be less than half of the distance.

Finally, the absolute difference between the wavelength observed and the emitted (from Nave list) needs to be less to $0.025\mathring{A}$. With larger differences the magnitude of the relative velocity doesn't make sense. This result is supported by the general observations made across the selection process.

3.2.2 Observational requirement

The last part of the selection was a visual inspection to discard line mixes or absent from the solar spectrum. The use of a visualizer application (explained in detail in the appendix C) was useful to see simultaneously the graphics related to dynamics aspects. Especially in the near infrared range. The visual requirement follows the observation of the geometry of the curve, behavior on plots and the guidance of professor Benjamin.

The final part of the methodology was to perform different plots for our analysis. This is based on the requirement for the characterization. First of all, the granulation pattern (relative velocity), core curvature and core bisector against line depth was performed to all ranges in both atlases with the objective to observe the three signatures of convection. Then, different plots were performed against line depth to characterize the phenomenon of chromodependence.

Chapter 4

Results and discussion: The three signatures of convection

Our results were separated into the three signatures of convection around the main phenomenon of chromodependence.

4.1 The first signature: Line broadening

4.1.1 Line depth-dependence on line core curvature

The core curvature was calculated following the equation (2.5) and plotted against line depth as shown in figure 4.1.
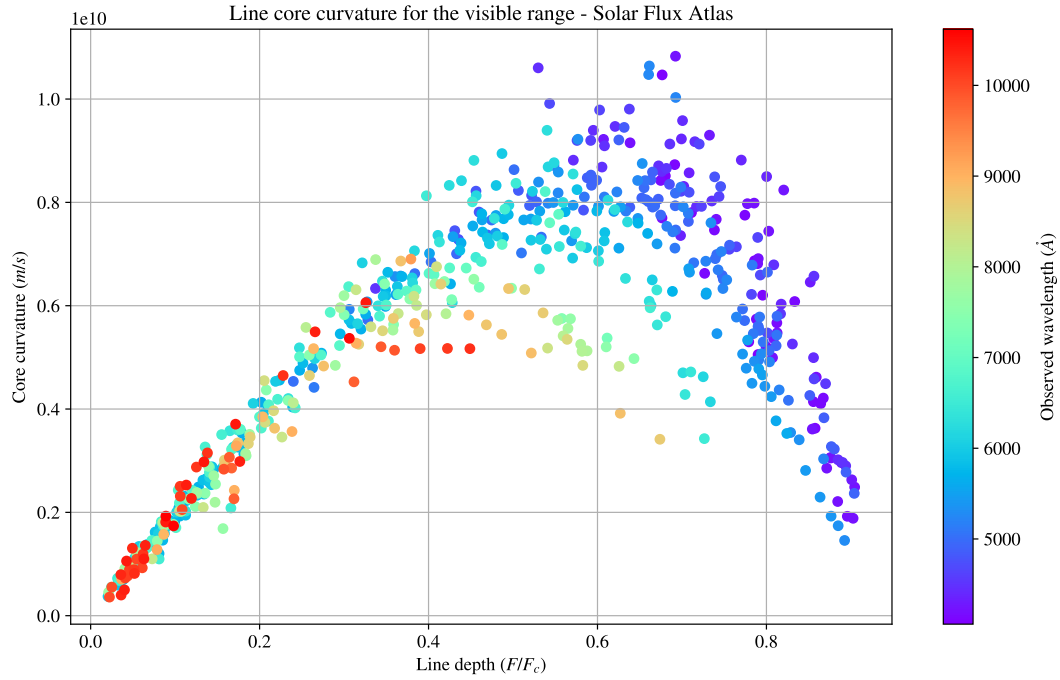
(a) Line core curvature for the visible range in the Solar Flux Atlas. Is visible a characteristic curve with line depth-dependence along wavelength.
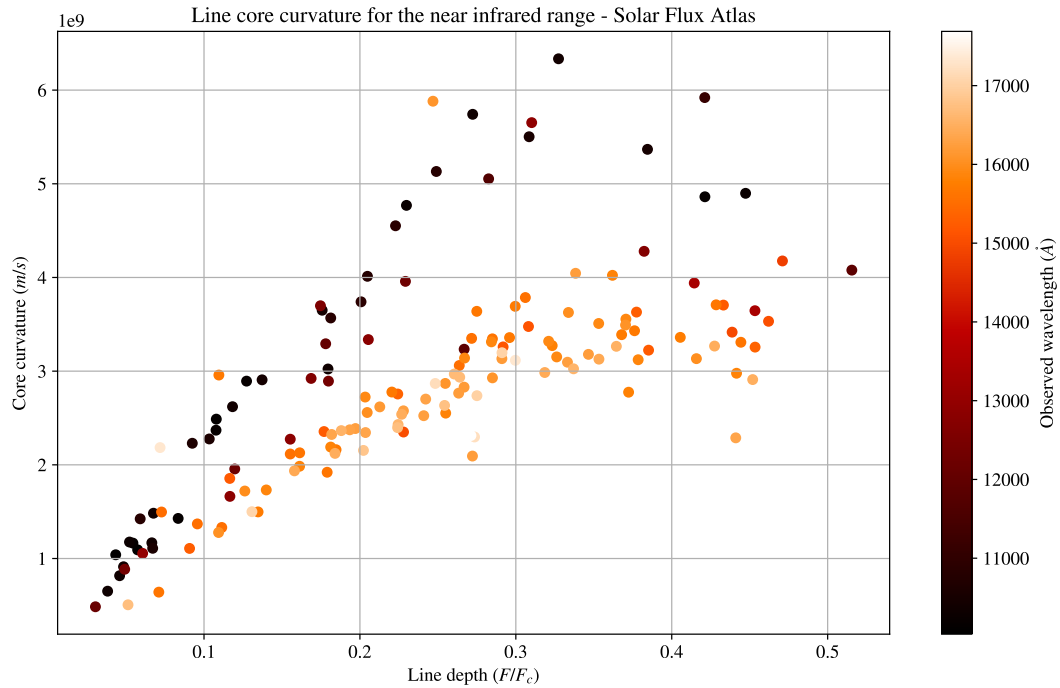
(b) Line core curvature for the near infrared range in the Solar Flux Atlas. Is visible a natural division for wavelengths in $11400\mathring{A}$.

Figure 4.1: Line core curvature for the Solar Flux Atlas separated in wavelength ranges.

As shown in the figure 4.1b for the near infrared range, is visible as a natural division for wavelengths in $11400\mathring{A}$, which corresponds to telluric lines of absorption in the atmosphere. Plotting all ranges of the Solar Flux Atlas is visible a line depth-dependence along wavelength.
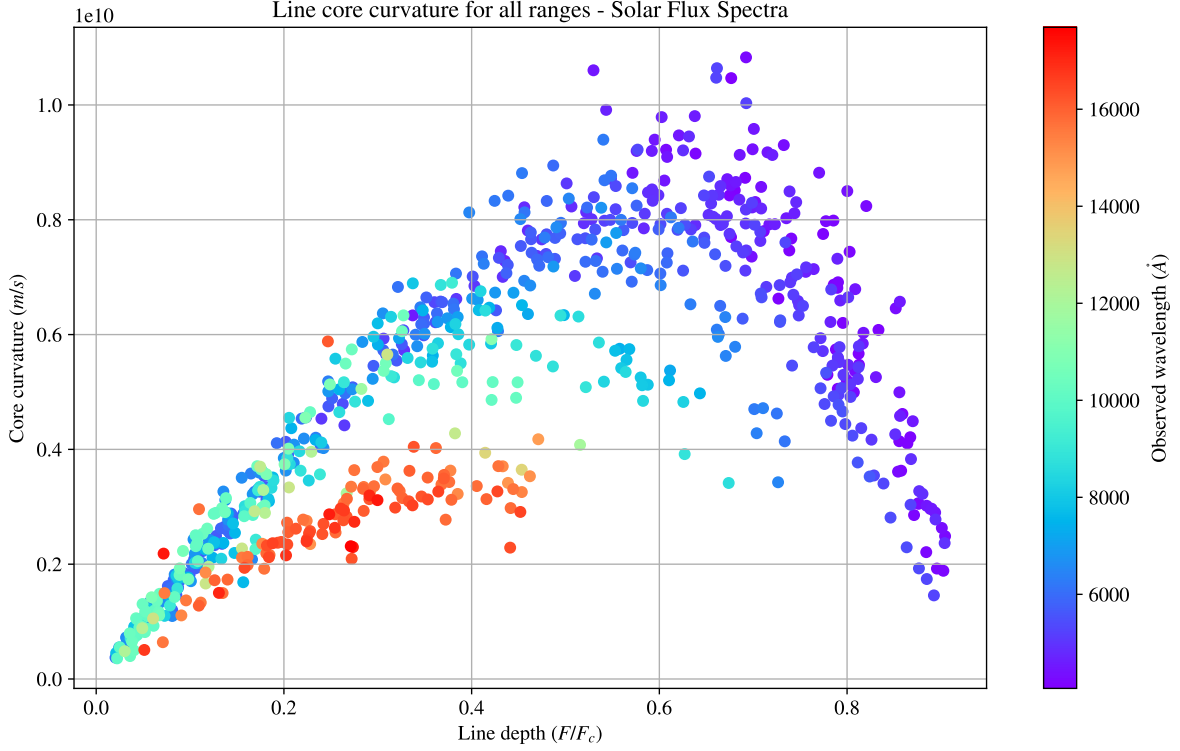
Figure 4.2: Line core curvature in the Solar Flux Atlas. The near infrared range presents a natural division due telluric lines in the atmosphere.

Despite the line depth-dependence shifts along wavelength is clear a linear tendency on the visible part of the atlas (see figure 4.2). Then, a first order polynomial fit was fitted to the range $0.0 - 0.1 F/F_c$ of line depth in the visible range of the Solar Flux Atlas where F/F_c represents the normalised flux.
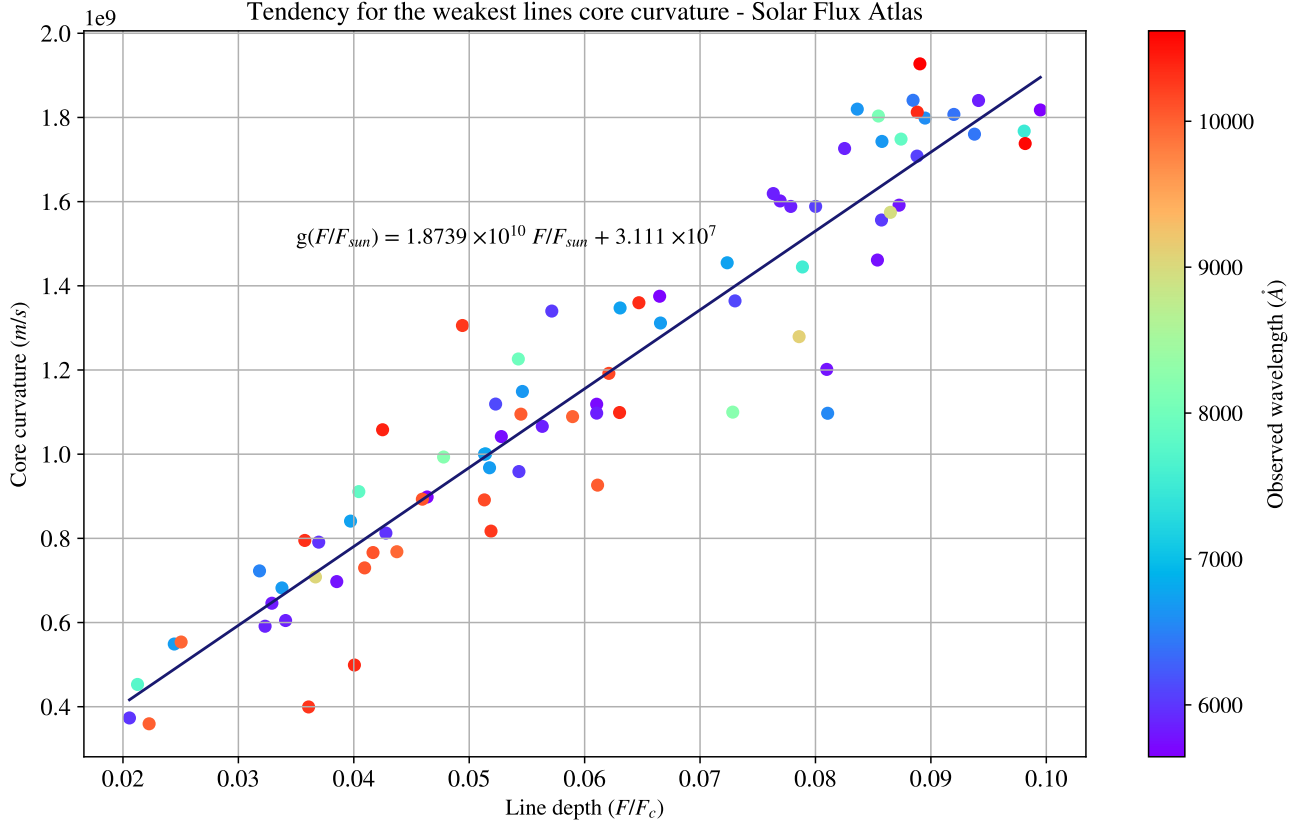
Figure 4.3: First order polynomial fit fitted to the range $0.0 - 0.1 F/F_c$ of line depth in the visible range of the Solar Flux Atlas.

As can be seen in figure 4.3, the slope has a value of 1.8739×10^{10}. Due to the fact of non-chromodependence in this range, can be concluded that line core curvatures have a net dependence of the velocities and a non-dependence caused by atomic effects. To confirm this statement, was plotted the line core curvature for the visible range in the Spatially Resolved Quiet Sun Atlas with $\mu = 0$ (see figure 4.4). In other words, was plotted the same behavior for the disk flux of the Sun center, this type of data don't present the effect of rotation.

Figure 4.4: Line core curvature for the visible range for disk center data from the Spatially Resolved Quiet Sun Atlas.

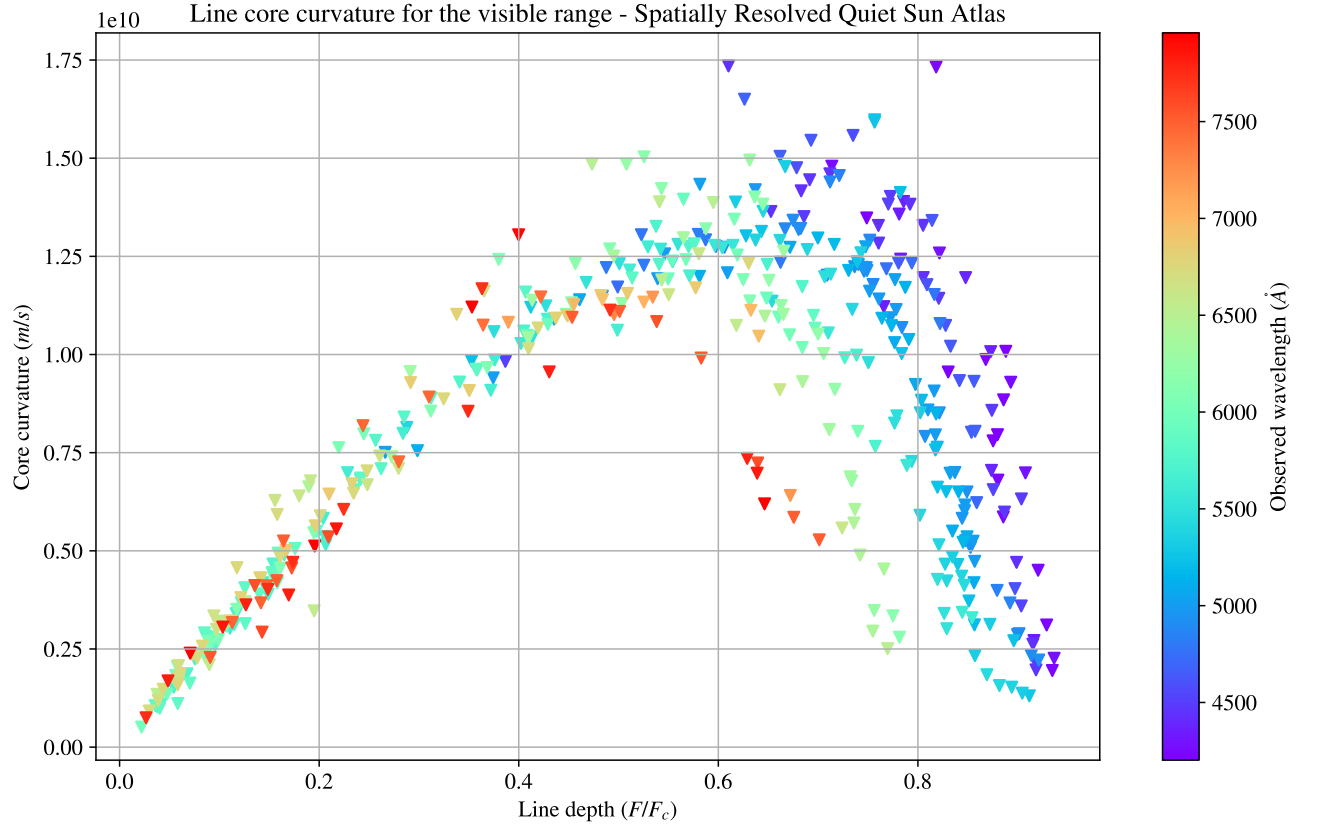As shown in figure 4.5 calculating the first order polynomial fit was found the value of 2.9360×10^{10} for the slope.
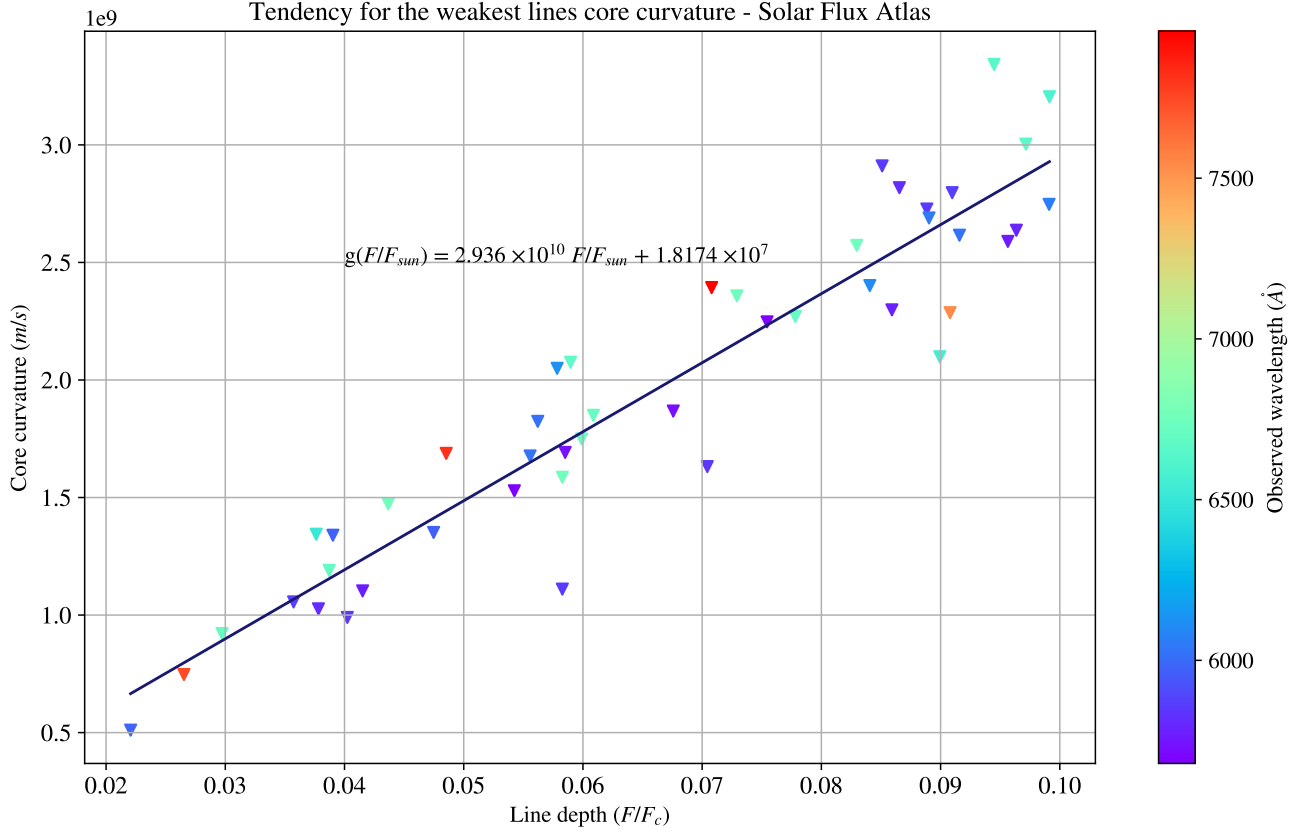
Figure 4.5: First order polynomial fit fitted to the range $0.0 - 0.1\,F/F_c$ of line depth in the visible range of the Spatially Resolved Quiet Sun Atlas.

This confirms the hypothesis that smallest line core curvature, or weaker lines, are displaced across the line depth as consequence of rotational Doppler effects. These weaker lines are known to represent the lower energy excitations. In consequence, the dependence of line depth with lower excitation energy was studied.

4.1.2 Line depth-dependence on lower excitation energy

The Nave list for Fe I lines [15] include the values for the highest and the lowest excitation energy. As shown in the figure 4.6 the relative velocity was plotted against lower excitation energy, where it is not clear a strong shift on the velocity.
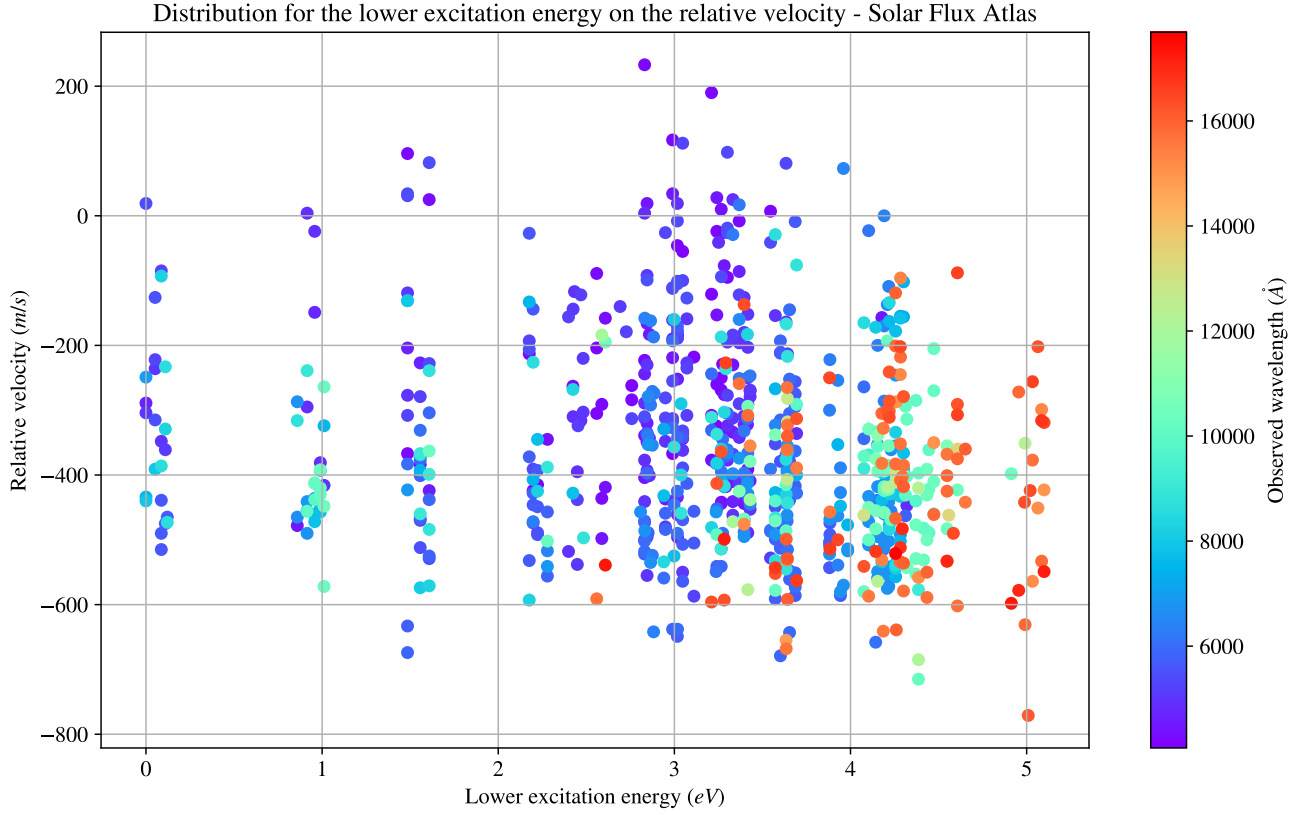
Figure 4.6: Relative velocity against lower excitation energy for all the range in the Solar Flux Atlas

However, when the relative velocity are separated on bins of $50m/s$ and plot the lower excitation energy against line depth it can be seen shifts in the energy as shown in figure 4.7.

Figure 4.7: Velocity bins of 50*m/s* across the figure 4.6, with this separation is visible the energy shift across line depth.

The figure 4.8 explicitly shows the dependency on the highest values for the lowest excitation energy across the wavelength, which can be fitted as a first order polynomial fit.

Figure 4.8: Individual plots of lower excitation energy across line depth representing each bin of velocity for the Solar Flux Atlas.

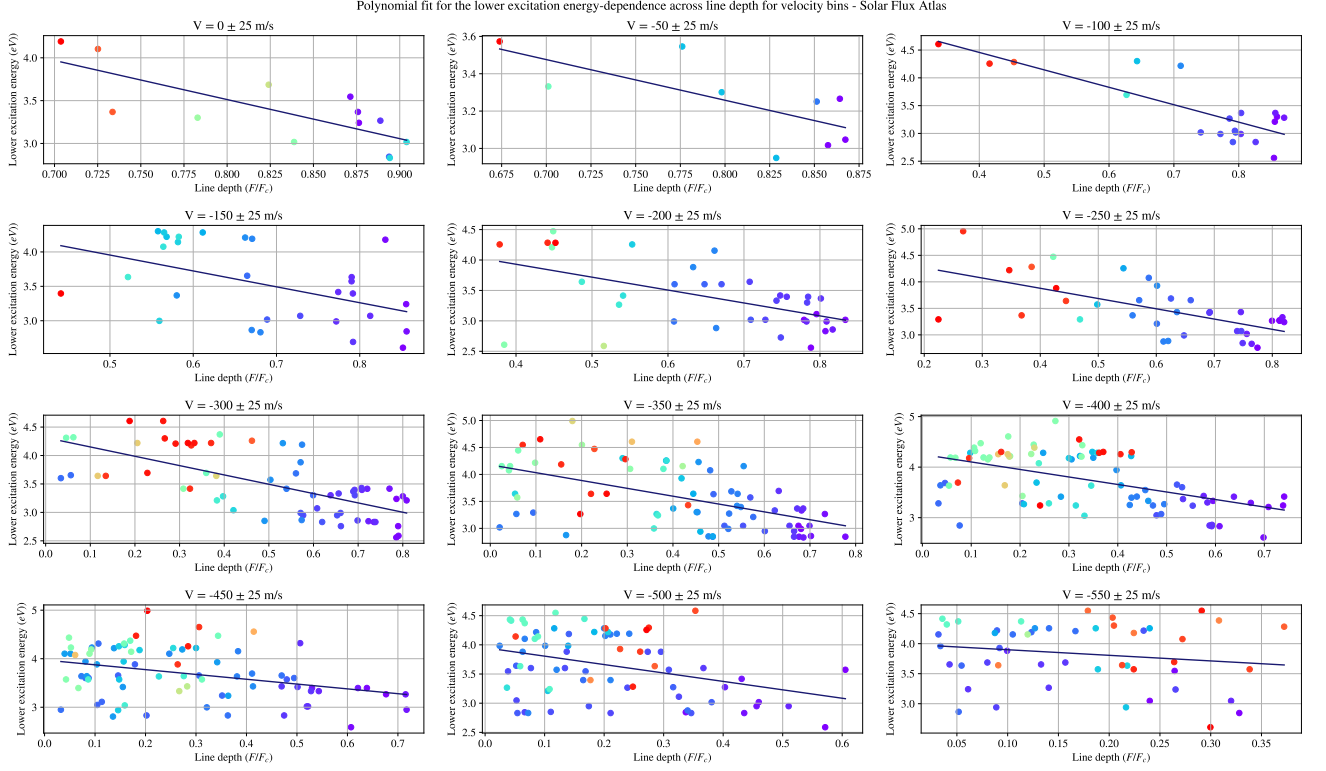For the range of velocity $-175m/s$ to $-525m/s$ the values for slopes are similar as shown in table 4.1, whose indicates the same ratio of shifts in the energy.

Velocity bin	Shift	Slope	Error slope	Error shift
0	7.1636	-4.5638	1.1564	0.9651
-50	5.0005	-2.1781	0.8069	0.6495
-100	5.7114	-3.1355	0.4958	0.3697
-150	5.1098	-2.3102	0.8208	0.5688
-200	4.7782	-2.1203	0.5594	0.3747
-250	4.6533	-1.9361	0.4121	0.2588
-300	4.3146	-1.6399	0.2408	0.1314
-350	4.1778	-1.4534	0.2694	0.1251
-400	4.2510	-1.4863	0.2683	0.1030
-450	3.9734	-0.9916	0.2973	0.0982
-500	3.9506	-1.4429	0.4428	0.1097
-550	3.9919	-0.9308	0.7750	0.1497

Table 4.1: Values for the coefficients on the first order polynomial fit adjusted on te different velocity bins.

To corroborate the only energy-dependence the same analysis was realized on the Spatially Resolved Quiet Sun Atlas for $\mu = 0$. The plot of relative velocity against lower excitation energy for this atlas presents the same behavior as the solar flux. However, performing the first order polynomial fits was found that the values of slopes are higher (see figure 4.9 and table 4.2).
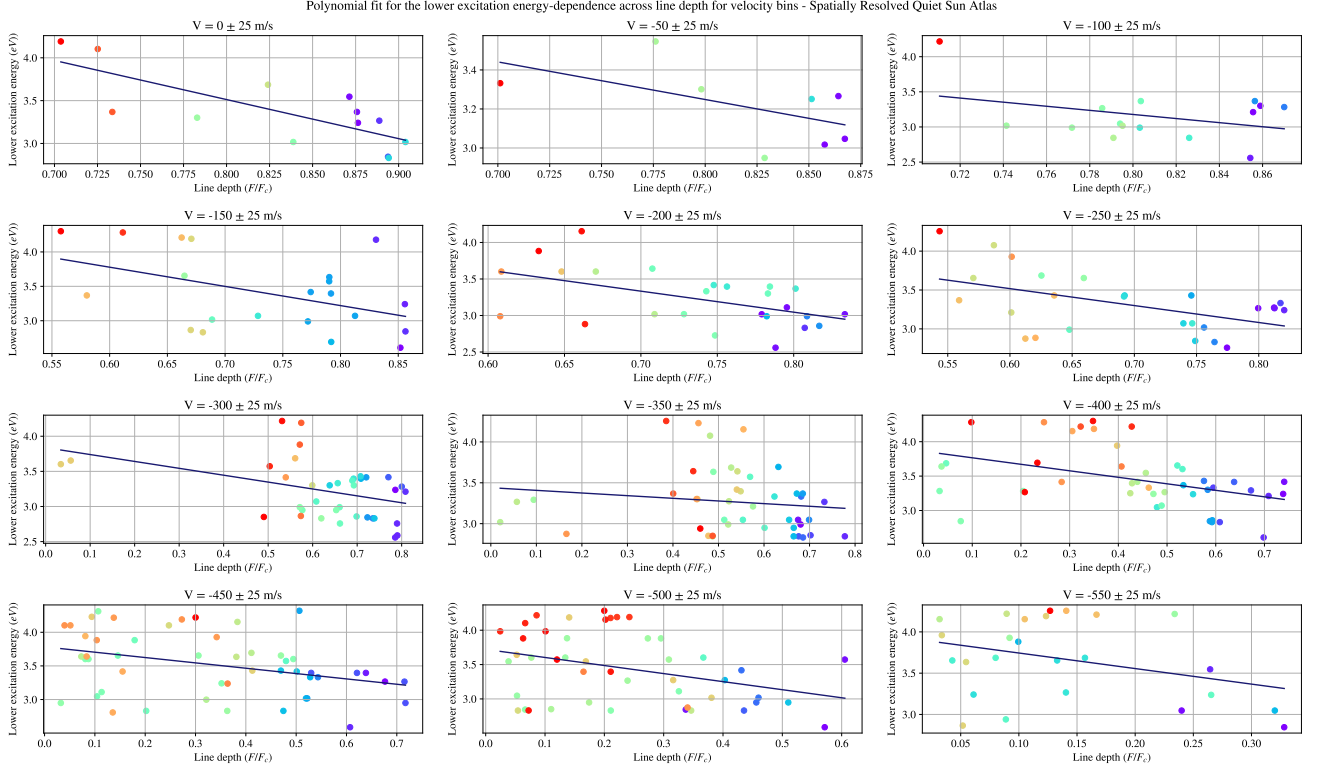
Figure 4.9: Individual plots of lower excitation energy across line depth representing each bin of velocity for the Spatially Resolved Quiet Sun Atlas.

Then, the rotational doppler affected the energy...(*argument on construction*)

4.2   The second signature: Line profile bisector asymmetry

4.2.1   The bisector slope

The line core bisector slope was calculated following the equation (**??**) and plotted against line depth as shown in figure 4.10.

Velocity bin	Shift	Slope	Error slope	Error shift
0	7.1636	-4.5638	1.1564	0.9651
-50	4.7903	-1.9274	1.1583	0.9496
-100	5.5099	-2.9149	2.0695	1.6744
-150	5.4525	-2.7907	1.2421	0.9195
-200	5.3471	-2.8771	0.9840	0.7277
-250	4.8238	-2.1774	0.7516	0.5241
-300	3.8374	-0.9802	0.3714	0.2419
-350	3.4399	-0.3246	0.3473	0.1931
-400	3.8607	-0.9455	0.3184	0.1511
-450	3.7832	-0.7942	0.3032	0.1174
-500	3.7206	-1.1728	0.4614	0.1291
-550	3.9324	-1.8835	1.0826	0.1770

Table 4.2: Values for the coefficients on the first order polynomial fit adjusted on te different velocity bins.
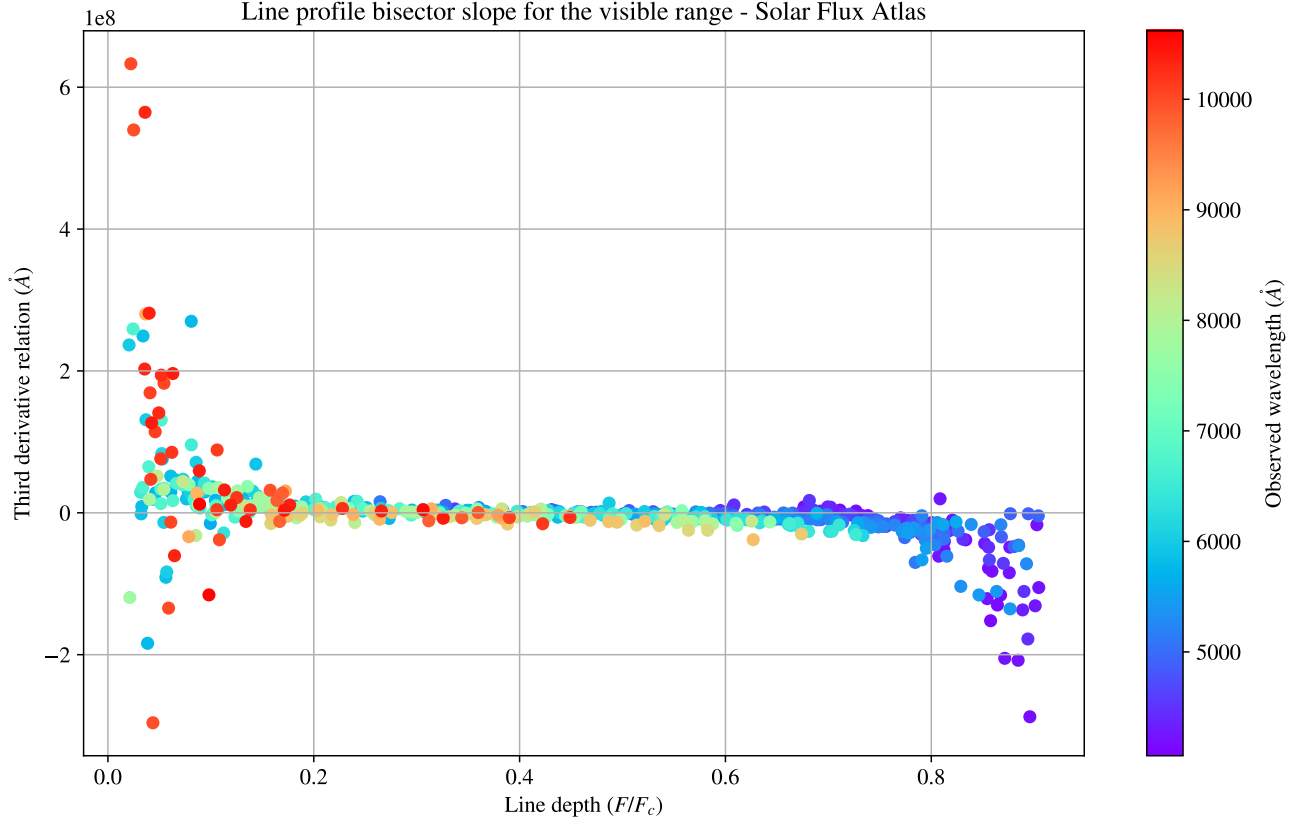
Figure 4.10: Line profile bisector slope for the visible range in the Solar Flux Atlas. The behavior of the plot is according to the C-curved shape of the line bisector affected by convection movement.

The weakest lines have a non c-curved profile bisector due to the small depth, so the bisector just shows an redshift or a slope. On the other hand, the lines which are more deeper in the photosphere experimenting the convective blueshift in its totality, so the slope had to be negative. However, the values for line depth which are in the middle represents equilibrium point where the convective cell overshoot come back due to gravitational forces. Then, a first order polynomial fit was adjusted to the range $0.3 - 0.6 F/F_c$ as shown figure 4.11.

Figure 4.11: First order polynomial fit adjusted to the range $0.3 - 0.6 F/F_c$ for the line bisector slopes.

For a point of comparision, the same analysis was realized to the disk center spectra (see figure 4.12).
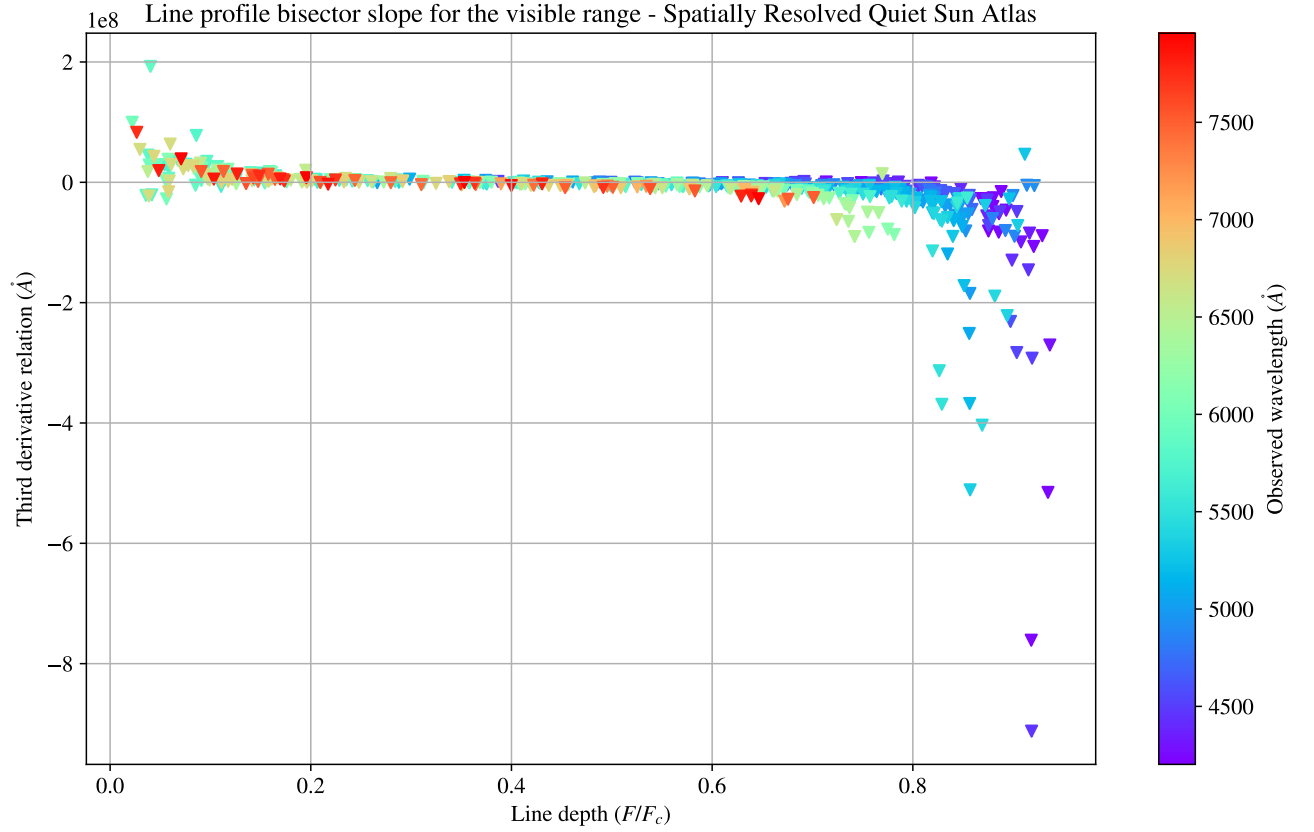
Figure 4.12: Line profile bisector slope for the visible range in the Spatially Resolved Quiet Sun Atlas.

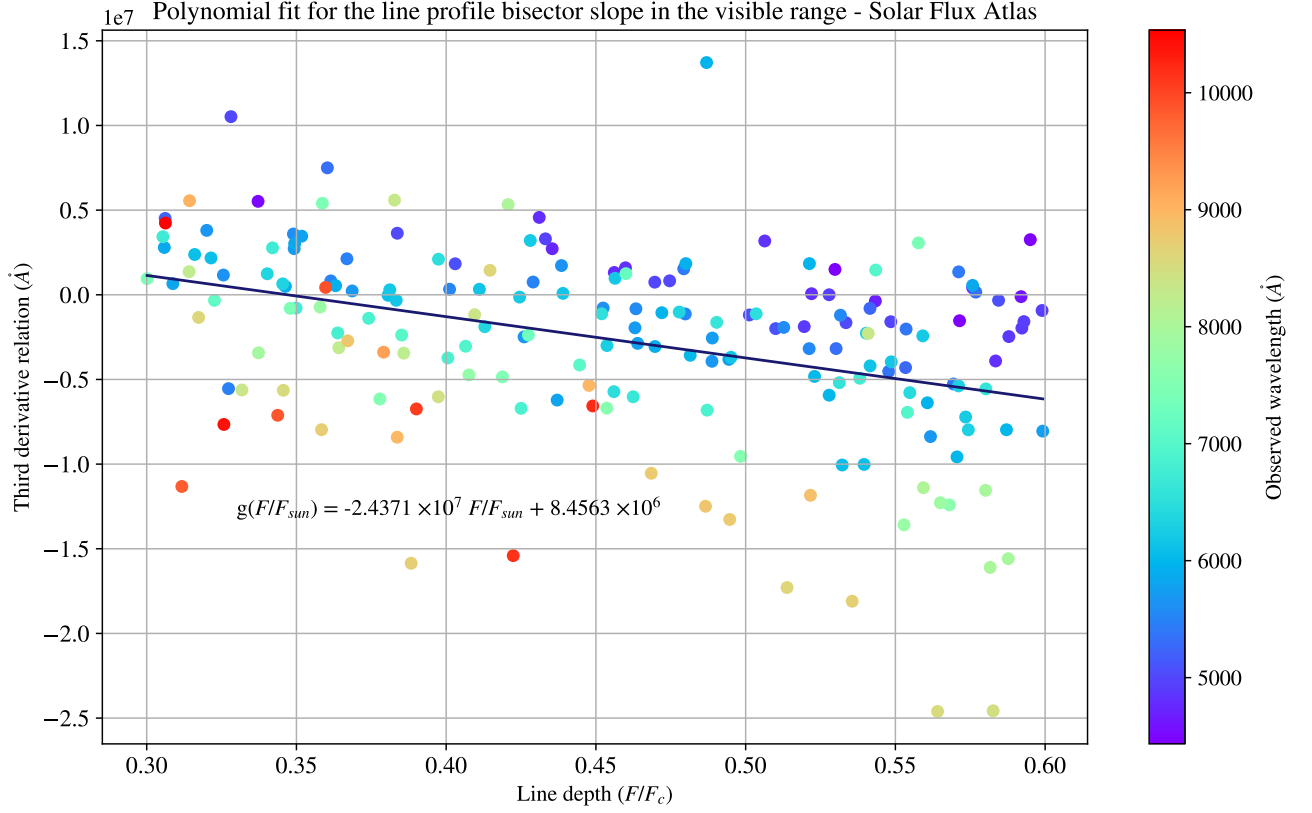Where the center disk shows a small slope than all integrated flux, but with the same behavior (see figure 4.13).
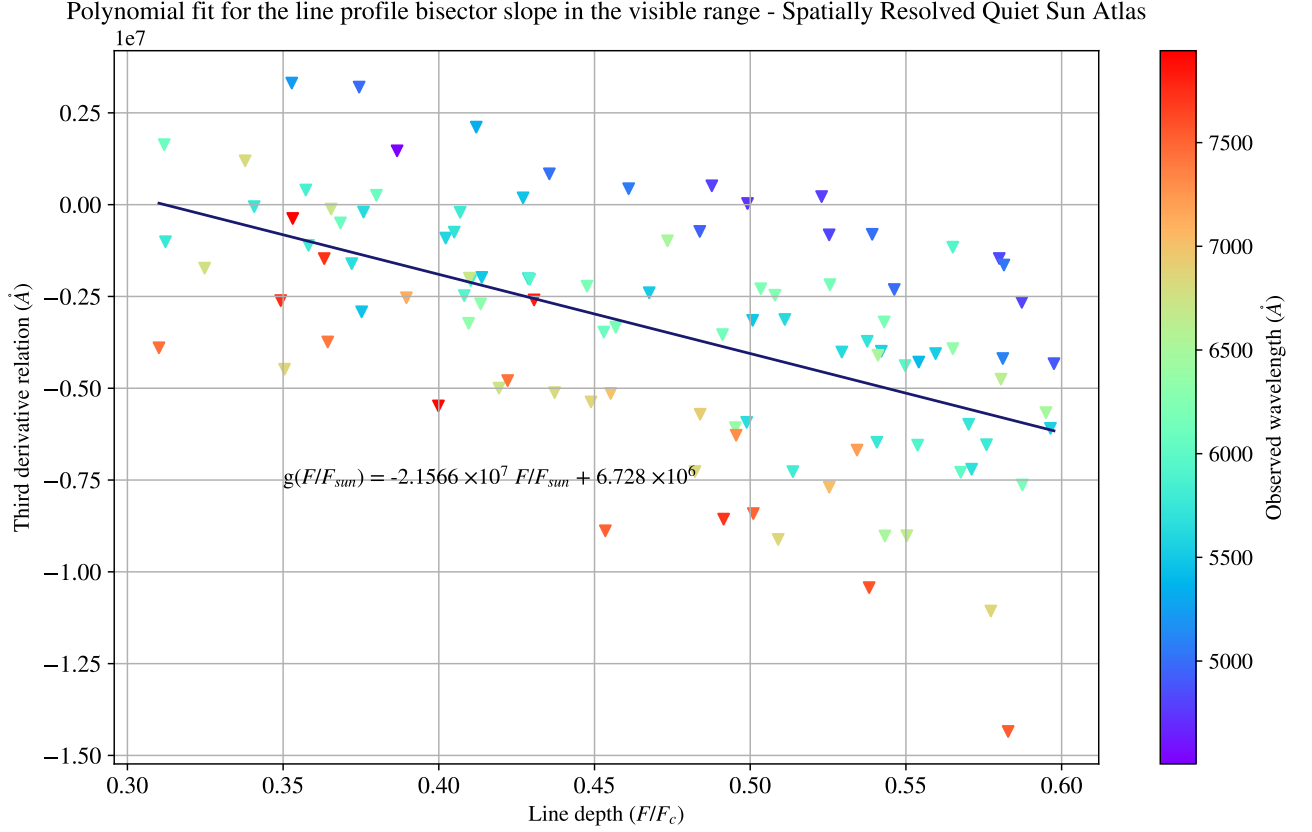
Figure 4.13: First order polynomial fit adjusted to the range $0.3 - 0.6 F/F_c$ for the line bisector slopes.

This leads us to...(argument in process)

4.2.2 Flux deficit (in progress)

Due to radiation, the redshift part of a line is displced on the flux, inducing a rotation on the c-curved profile bisector. This phenomenon is called flux deficit. Hamilton and Lester [9] noticed that the behavior of the third signature mimics the bisectors gives the sight of the mean bisectors following the granulation pattern behavior, this last is discussed in the next section. Later, Gray and Oostra [7] show that the bisectors need to follow the granulation pattern as the form of we calculated velocities and bisectors.

For comparision with Gray and Oostra work, was taken the line $6254.2850\mathring{A}$ as shown in figure 4.14.
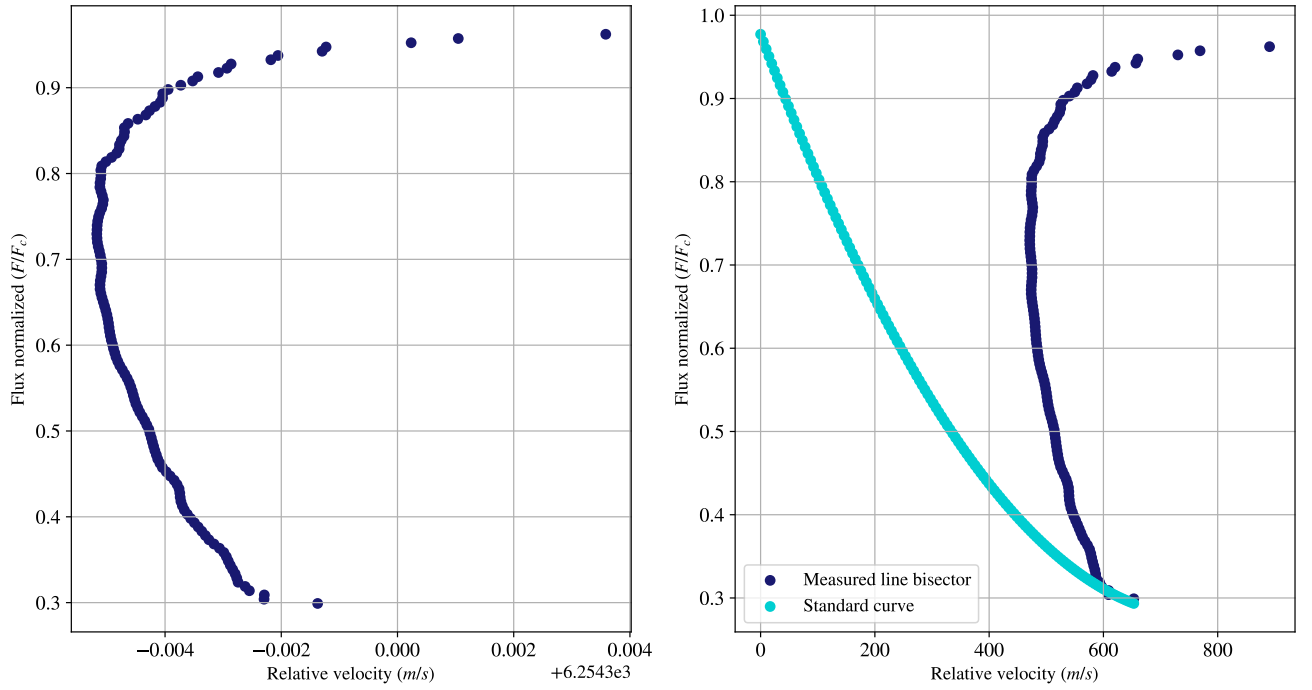
Figure 4.14: C-curved line profile bisector for the $6254.2850\mathring{A}$ and the standard curve for the green range from the third signature plot.

Following the same method, the figure 4.15 shows a flux imbalance described on the distribution and temperatures of the mean, the maximum and the RMS point of the bisector.

Flux deficit curve for 6254.2850 $\mathring{A}$
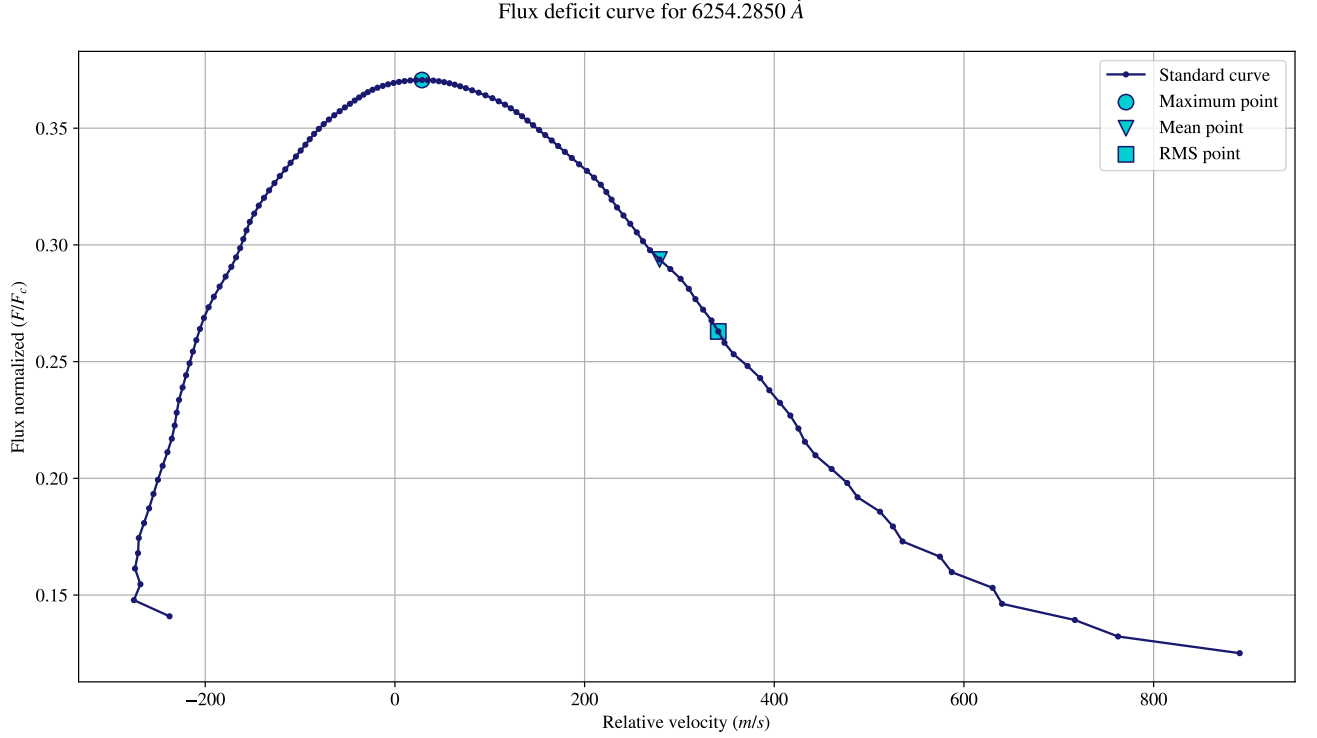
Figure 4.15: Flux deficit curve for the 6254.2850$\mathring{A}$ and the temperatures of the mean, the maximum and the RMS point of the bisector.

Taking the model on Gray [16], the respective temperatures are ().

As we found the standard curves for all the ranges, the same analysis was realized for a random line in the range of the respective standard curve.

4.3 The third signature: Line depth-dependence on wavelength shifts

4.3.1 The granulation pattern

The granulation patterns for the IAG Solar Flux Atlas in all the wavelength range was obtained.
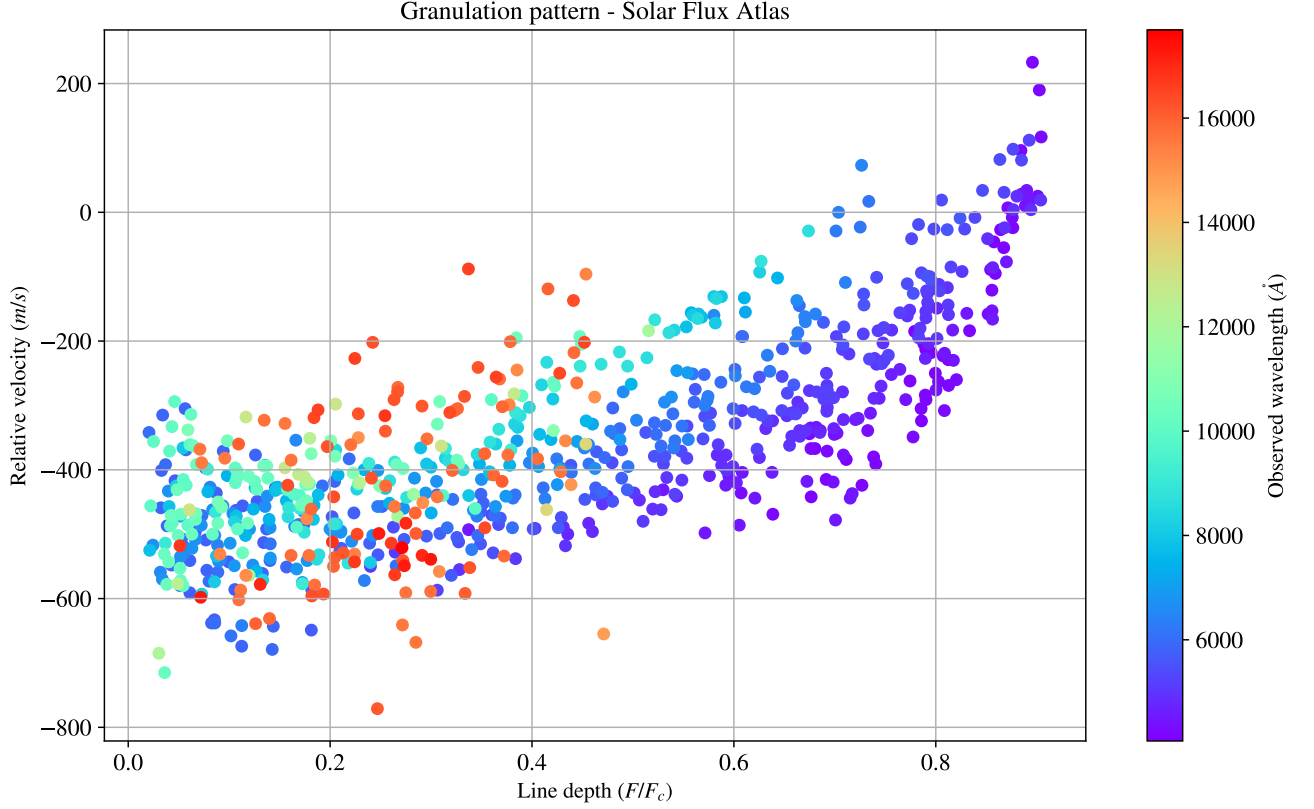
Figure 4.16: Granulation pattern obtained for the Solar Flux Atlas. The wavelength shift dependence is along the line depth.

As shown in the figure 4.16 the behavior along the line depth is according to literature, in which is clear the wavelength shift dependence along the line depth or chromodependence. For a description of this tendency was performed an analysis of line depth against wavelength. The hypothesis was: "If there exists a velocity shift only in the Solar Flux Atlas, then rotation could be the cause of this phenomenon." However, the velocity shift was observed in both spectral datasets. This was initially unexpected because the rotation is negligible at the disk center.

For the measurement of wavelength shifts a range from $4300\mathring{A}$ to $5600\mathring{A}$ was taken. Then was sorted all wavelengths from both atlases into $50m/s$ velocity bins (see figure 4.17).
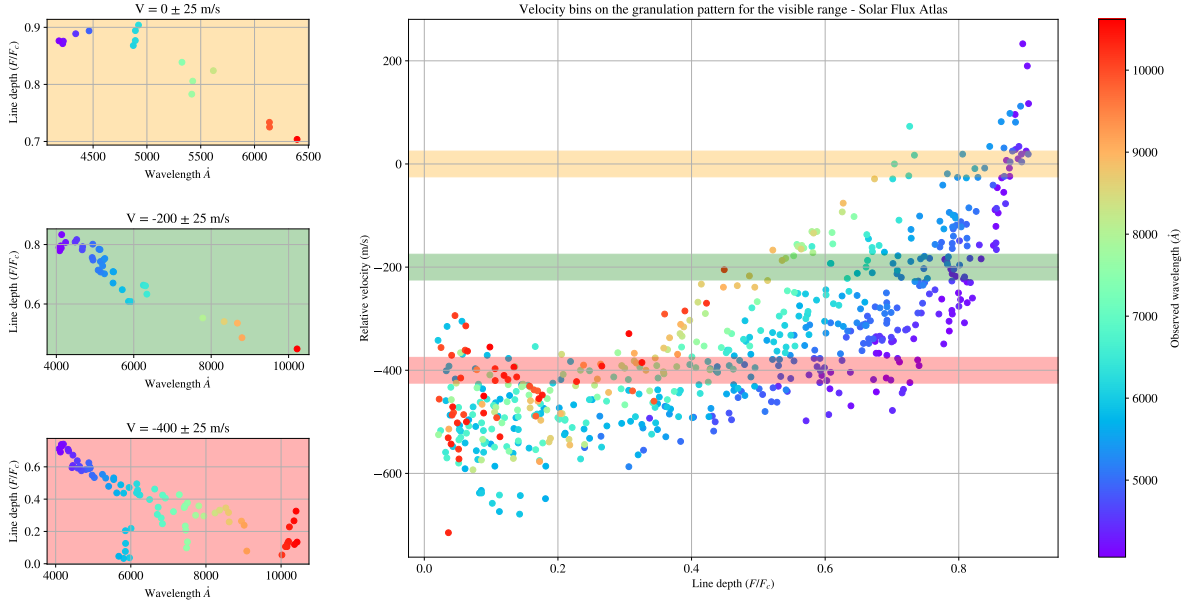
(a) Visible range for the Solar Flux Atlas.
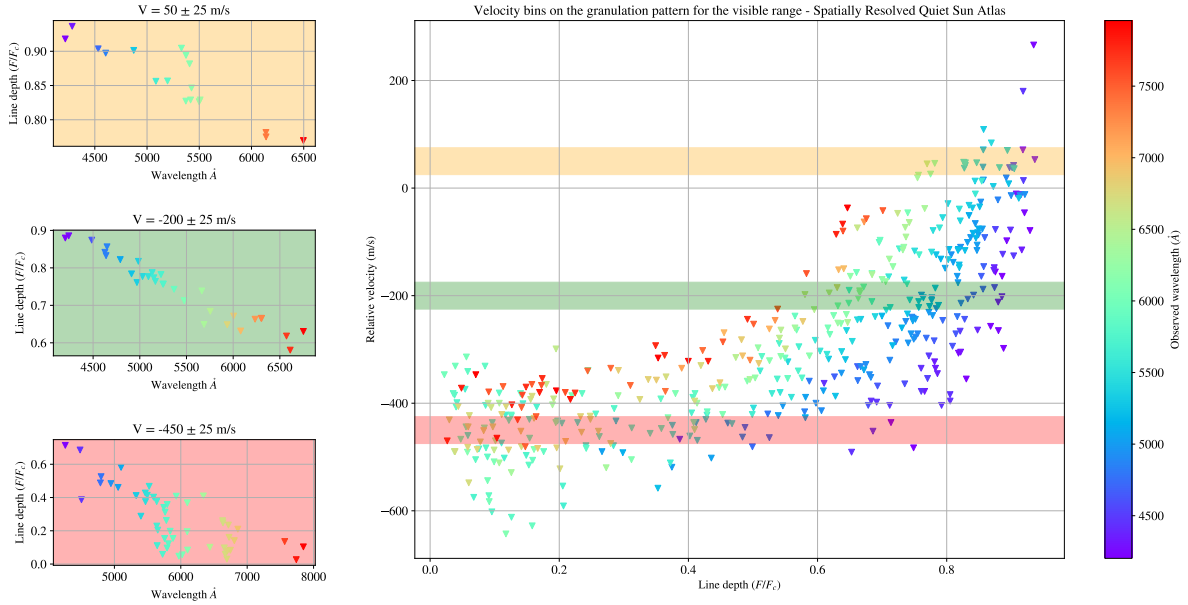
(b) Visible range for the Spatially Resolved Quiet Sun Atlas.

Figure 4.17: Comparision between atlases with velocity bins for the relation between wavelength and line depth. For each velocity bin was plotted wavelength against line depth to measure a frequency shift with a first order polynomial fit.

For each velocity bin was plotted wavelength against line depth to measure a frequency shift

with a first order polynomial fit (see figure 4.18)
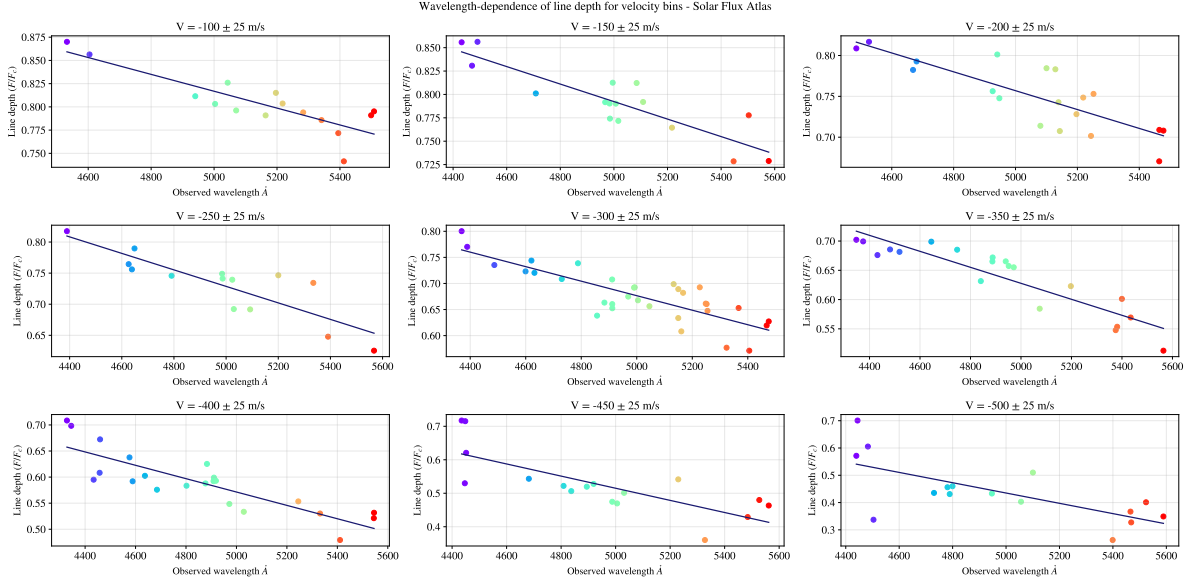
(a) Velocity bins of $50 m/s$ for the Solar Flux Atlas.
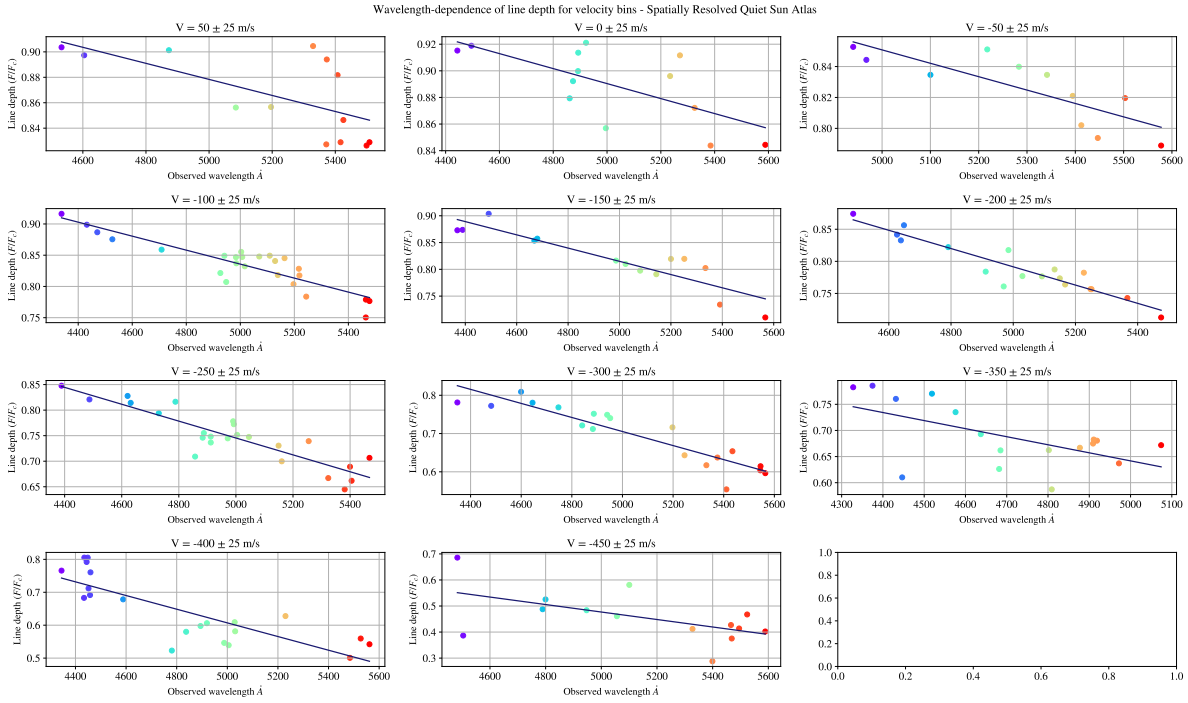
(b) Velocity bins of $50 m/s$ for the Spatially Resolved Quiet Sun Atlas.

Figure 4.18: Individual plots of lower excitation energy across line depth representing each bin of velocity.

The tables 4.3 and 4.4 shows the obtained slopes in both atlases.

Velocity bin	Shift	Slope	Error slope	Error shift
50	1.1937	-0.000063	0.000022	0.1166
0	1.1720	-0.000056	0.000018	0.0923
-50	1.2840	-0.000087	0.000021	0.1087
-100	1.3953	-0.000112	0.000012	0.0584
-150	1.4327	-0.000124	0.000017	0.0842
-200	1.5028	-0.000142	0.000013	0.0658
-250	1.5712	-0.000165	0.000018	0.0890
-300	1.6233	-0.000184	0.000019	0.0971
-350	1.4129	-0.000154	0.000055	0.2583
-400	1.6455	-0.000208	0.000033	0.1617
-450	1.1952	-0.000144	0.000060	0.3094

Table 4.3: Slopes for the first order polynomial fit in each velocity bin for the Spatially Resolved Quiet Sun Atlas.

Velocity bin	Shift	Slope	Error slope	Error shift
-100	1.2704	-0.000091	0.000015	0.0797
-150	1.2601	-0.000094	0.000013	0.0673
-200	1.3340	-0.000115	0.000019	0.0985
-250	1.3920	-0.000133	0.000023	0.1164
-300	1.3724	-0.000139	0.000017	0.0874
-350	1.3106	-0.000137	0.000015	0.0744
-400	1.2119	-0.000128	0.000018	0.0866
-450	1.4212	-0.000181	0.000039	0.1947
-500	1.3787	-0.000189	0.000052	0.2609

Table 4.4: Slopes for the first order polynomial fit in each velocity bin for the Solar Flux Atlas.

The value of slopes for the Spatially Resolved Quiet Sun Atlas are greater than the Solar Flux Atlas, which contradicts the initial hypothesis.

4.3.2   Characterization of chromodepence on granulation pattern

The figure 4.19 show the standard curve proposed for Gray and Oostra [7], stablish on the range $6020 - 6340 \mathring{A}$
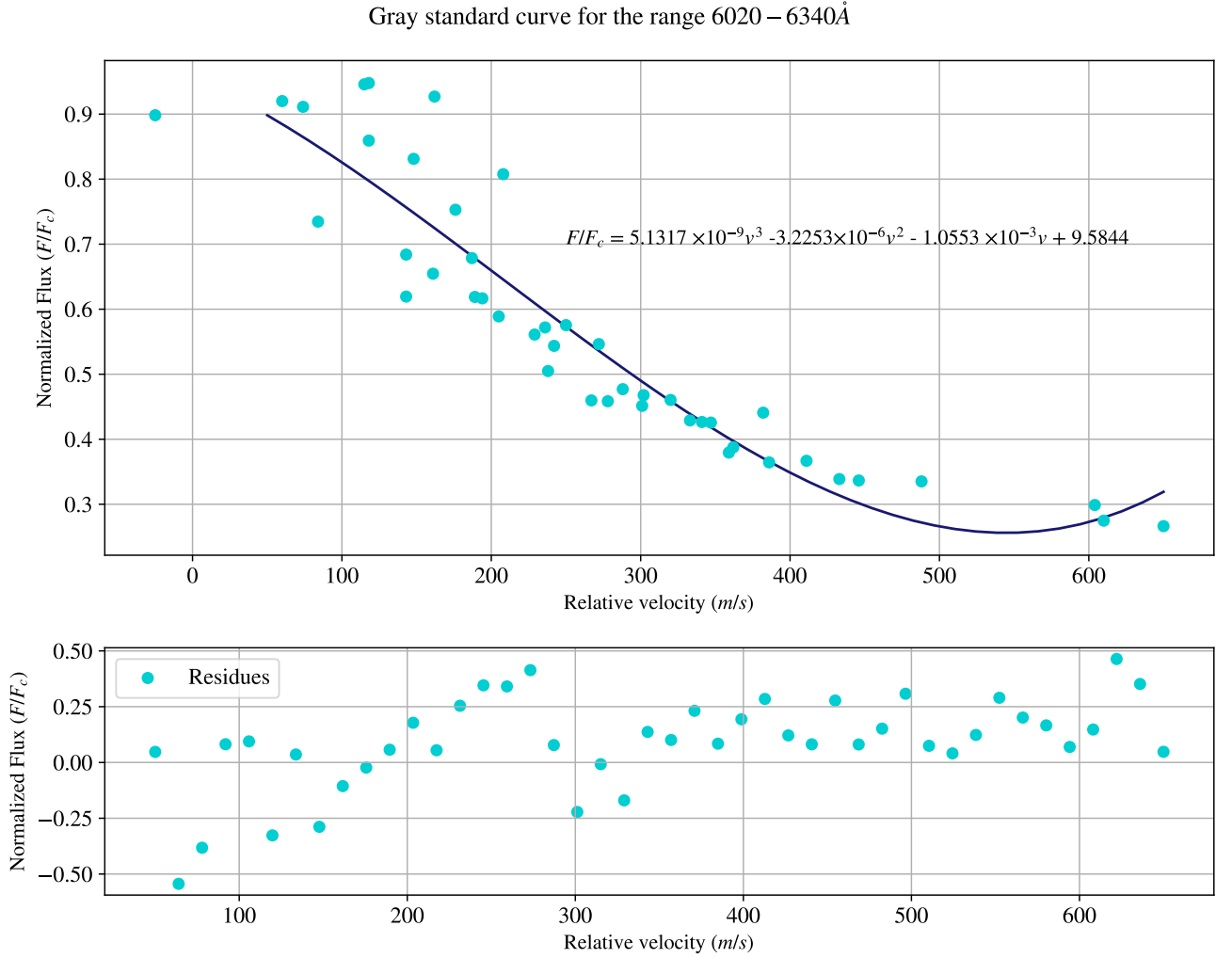
Figure 4.19: Standard curve given by Gray and Oostra and recalculated for comparision with the current work.

As the standard curve don't take into account all the wavelengths and the given third order

polynomial fit overstimate the points, a different approach was proposed. Separating into color ranges, a second order polynomial fit was adjusted.
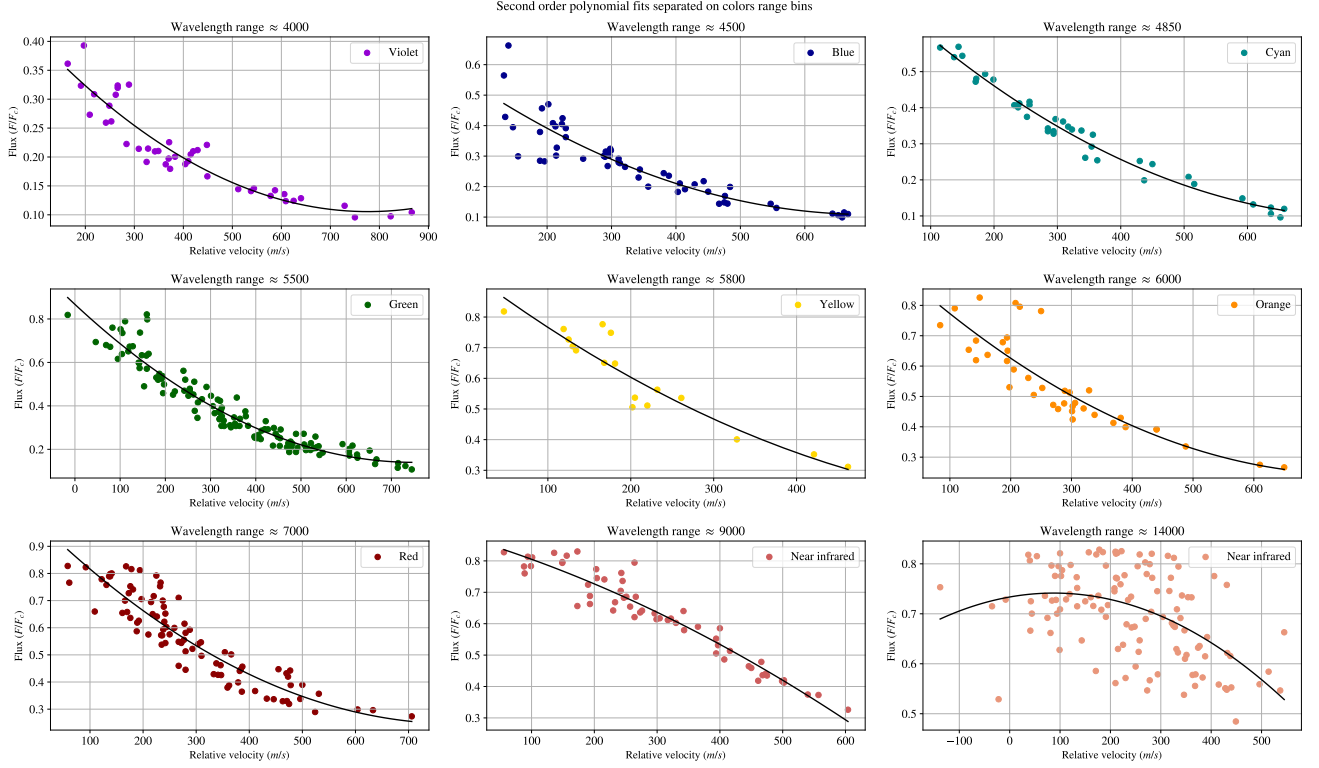
Figure 4.20: Granulation pattern for the Solar Flux Atlas with color curves. The tendency on the curves is more pronounced in the violet and red range.

The tendency on the curves is more pronounced in the violet and near infrared range (see table 4.5). This can be interpreted as the standard curve from Gray and Oostra is shifted and flattered along decreasing wavelengths.

Wavelength range ($\mathring{A}$)	Color coefficient
3800-4270	4924.2052
4270-4760	757.0966
4760-4970	263.3435
4970-5700	204.8798
5700-5810	155.9806
5810-6180	190.1927
6180-7800	142.9648
7800-11000	160.4951

Table 4.5: Values for the second order polynomial fit coefficients shown in figure 4.20.

Taking the curve for the range $4970-5700\mathring{A}$ for the starting point or "standard curve" different scaling coefficients wer calculated as shown the table 4.6.

Wavelength range ($\mathring{A}$)	Color coefficient
3800-4270	0.5359
4270-4760	0.8195
4760-4970	0.8348
4970-5700	1.000
5700-5810	1.0595
5810-6180	0.9834
6180-7800	1.0149
7800-11000	0.2857
11000-23000	-0.0115

Table 4.6: Scaling factors to the new standard curve shown in the equation (4.1).

The equation (4.1) reports a new standard curve which coefficients depends on the color, and give the corresponding granulation pattern curve for each color range exposed on the table 4.6.

$$F/F_c = 1.2925 \times 10^{-6} \alpha_c v^2 - 0.0019 \alpha_c v + 0.8671 \alpha_c \tag{4.1}$$

The near infrared range dont show the same tendency...

4.4   Higher quality graphs

To show the improvement on the quality in the third signature plots, the figure 4.21 compare the plot obtained by Ellwarth [6] and the graphic.
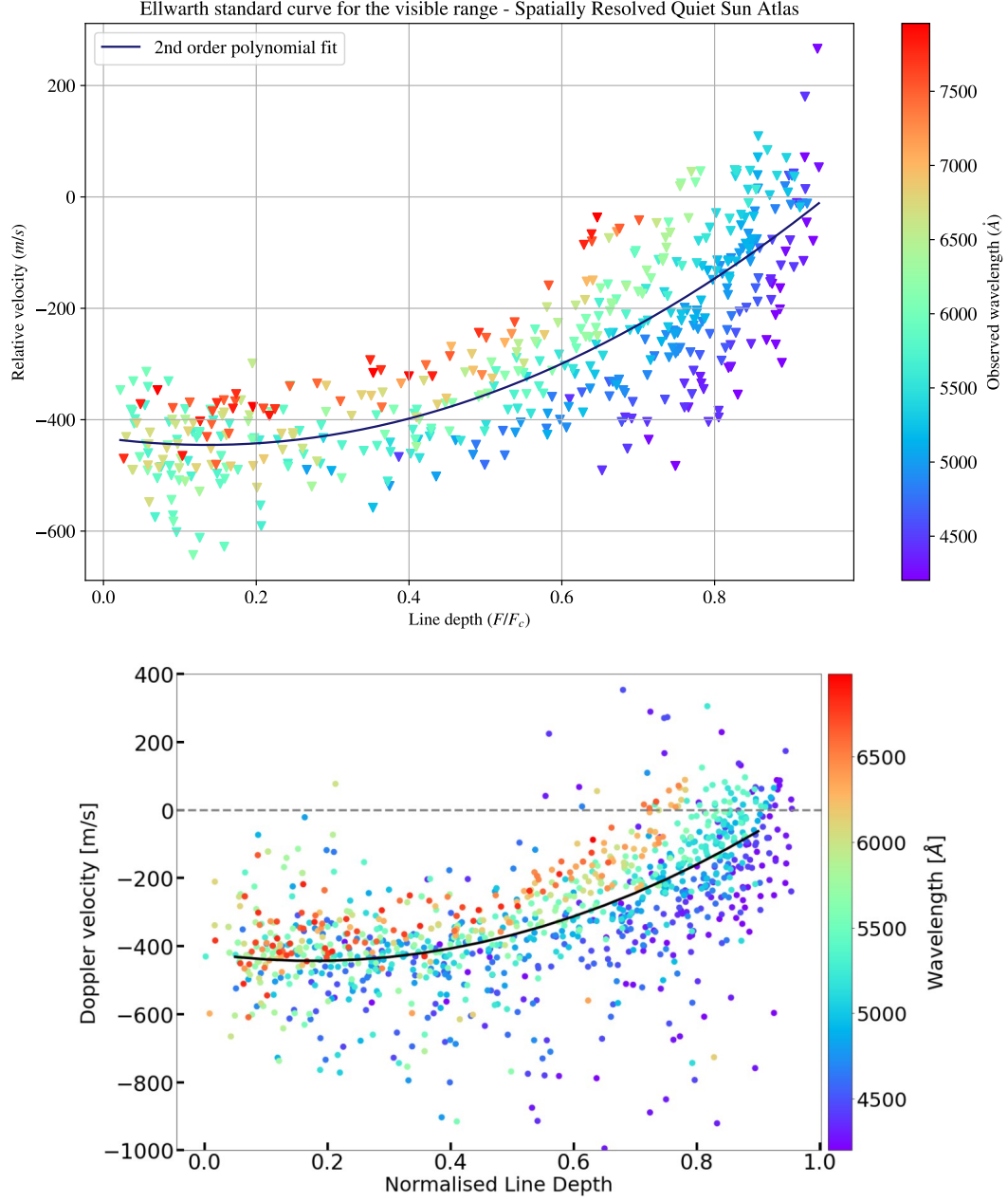
Figure 4.21: We realized the same graphic for the comparision with the Ellwarth article to show the less scattered points.

The less scattered points and the improvement on the chromodepence identification is evident. Furthermore, the variance of the observed wavelength was analysed altering the number of points on the fourth order polynomial fit. The figure 4.22 shows that is a good parameters until takes the infrared, where the number of points for line core is reduced comparing to a random

line in the viisble.
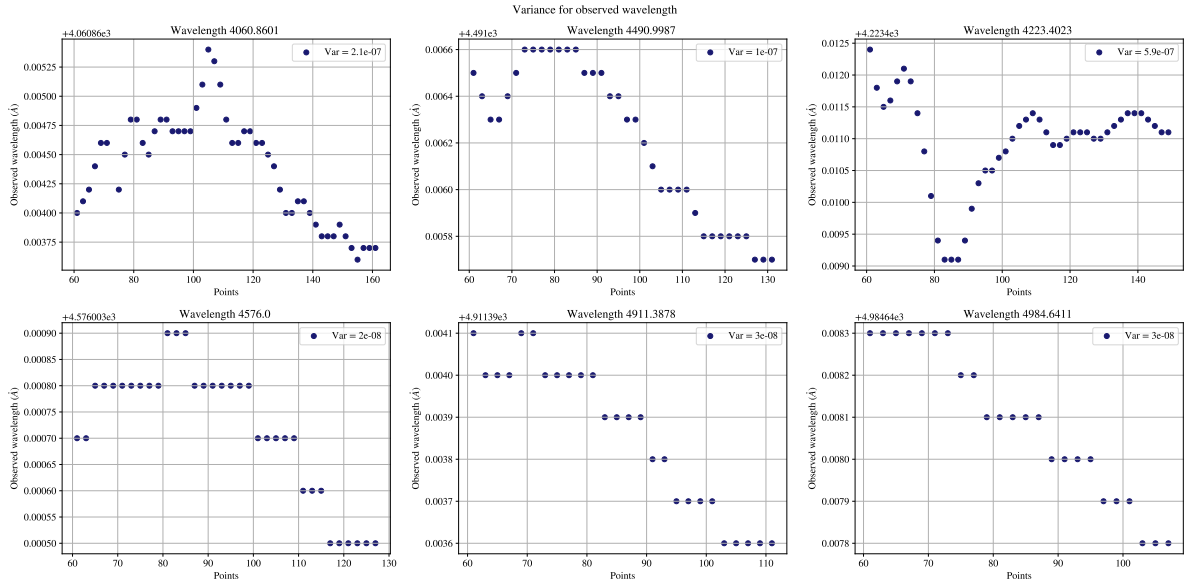
(a) Variance for random lines in the visible range for the Solar Flux Atlas.
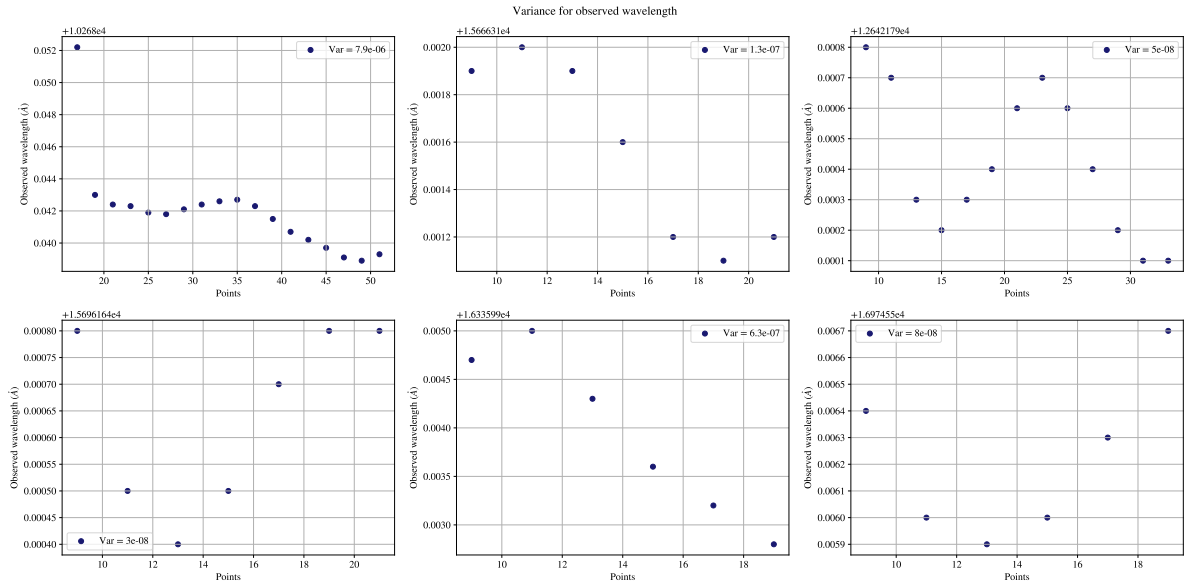
(b) Variance for random lines in the near infrared range for the Solar Flux Atlas.

Figure 4.22: Variance of the observed wavelength altering the number of points on the fourth order polynomial fit

This can proof that we do a good job?...

Chapter 5

Conclusions

In conclusion, a characterize the convective blueshift of solar absorption lines and its dependence on line depth and wavelength range was realized.

In specific, we produce a blend-free list of Fe I absorption lines and solar granulation patterns with minimal scatter. We describe in detail how the granulation plot depends on wavelength range. We explore possible explanations of wavelength-dependence and found thats () is the best. We explore ways of dealing with the wavelength-dependence when using the solar spectrum as a gauge for stellar spectra.

Appendix A

Z-score Standardization

In the process of calculate the four order polynomial fit the function np.poly.fit() presents an overstimation on the coefficients, due to the large difference of magnitude order between axis. To deal with this difference a z-score standardization was used on the selected bins of wavelengths around the observed wavelength. This process helps to avoid the dominance of certain features over other due to diferences in their scales [17].

The follow up for the standardization was applied the relation (A.1) on the selected bins for wavelength.

$$\lambda_{scaled} = \frac{\lambda - \mu(\lambda)}{\sigma(\lambda)} \tag{A.1}$$

Where $\mu(\lambda)$ refers to the mean and $\sigma(\lambda)$ to the standard deviation of the wavelength range. As the wavelength was scaled, in terms of calculated derivates for the first and the second signature, a re-scaled for this values was necessary. Based on the definition for the standardization, the derivates follow the relation (A.2).

$$\frac{d}{d\lambda} = \frac{1}{\sigma(\lambda)} \frac{d}{d\lambda_{scaled}} \tag{A.2}$$

Taking the derivate of the expresion (A.1) a factor related to the standard deviation appear. With this, the original values for derivates evaluated in the observed wavelength are expresed in equation (A.3)

$$\frac{d^2}{d\lambda^2} = \frac{1}{\sigma(\lambda)^2} \frac{d^2}{d\lambda^2_{scaled}} \qquad \frac{d^3}{d\lambda^3} = \frac{1}{\sigma(\lambda)^3} \frac{d^3}{d\lambda^3_{scaled}} \qquad (A.3)$$

This improved considerably the precision in the fit and there over the precision on the observed wavelength calculated.

Appendix B

The third derivate relation

Or called the bisector slope. It was multiplied by the relation ($\frac{c}{\lambda}$) to see each clear in the graphic.

Appendix C

Visualizer for outliers

For the process of the blend-free list was created an app using the interface Tkinter with the objective to help the visualization of outliers. Two versions of the visualizer were created. One just shows the line core and fourth order polynomial fit as shown in the figure ().

This helps for a first process where far separated lines were discarded. Then, we can perform the different calculations (core curvature, velocity and bisector slope), and use the second version of the visualizer (see figure ()).

In this version it can visualize the three signatures of convection and the line core with the fit. Moreover, was resalted the corresponding Fe I line on each graph to corroborate the behavior. Thanks to this software the time expended seeing lines was reduced significantly. Specially cause count with his own system to classification, adding lines to a Dataframe and save the image. Following the motivation we present the software on GitHub and its explained below.

C.1   Test example

The main code is in the file Visualizer.ipynb and the test example data are test.xlsx, feel free to change the type of data, the important is make a dataframe where the columns are [Wave , Flux] wavelength on Armstrong and flux normalized preferred. Then made another dataframe with the list of lines of Fe I.

The function closer lines select the closer minimums of the FeI lines and save the wave flux of

that minimum point and the Fe I line associated. Don't be confused, this is not the observed wavelength. This point is a reference for selecting the bins around the Fe I line. The function discards distances over 0.001A.

Then the function local points select the bins of each corresponding to one index on the closer lines dataframe. Each bin of wavelength is for 0.1mA around the minimum point.

The function Derivatives find the polynomial fourth order fit and calculate the minimum point with the fit, that is the observed wavelength. This returns a dataframe with the FeI line, flux fit and the minimum observed.

In parallel are calculated the bisectors of each line following the midpoint method, where equal points of flux are selected for comparison.

From this is the first visualizer that receives the local points, the values and the fit. This shows the line core and the fourth polynomial fit, in parallel is shown the bisector of each line in terms of velocity.

We recommend eliminating the lines that follow one of the conditions presented below: 1)The bisector doesn't show a C-curved bisector or it's too affected by the noise. 2)There is no curve or polynomial fit. This can be interpreted as the position on other points to the fit. 3) There's too much noise on the original line.

With this first filter the number of possible lines are reduced for calculating derivatives.

The second part of the code calculates the granulation pattern, core curvature and bisector slope. With these values the visualizer shows all the graphics including the line profile with the polynomial fit. In each graphic of derivatives the corresponding Fe I is resalted, this with the finally to select lines depending on his behavior.

This is a code test: Run the file test, you can adapt this part on your necessaries. The idea is the Dataframe results have the columns Wave (cm), nFlux and Wave A (there's no need for the flux to be normalized, it cannot be, we test this on arturus).

Then run the nave list, the present github has the table organized on an excel.

Run the cell of closer points and local points, the first needs to be returned a Dataframe and the other a list of dataframes.

For the first filter code you need to have a dataframe with the columns (), the list of local points

and the closer lines associated with the Dataframe, the fit values and the covariance values.

Modified this line to call the first visualizer.

Then, this part helps to extract the Dataframe with the lines that don't behave like the condition parameters. This can also help to drop the unnecessary lines

For the second enter the file with the lines resulting in the first filter, and run again the code for closer lines and local points, and then the second big filter.

Modified this line to call the second visualizer.

The next line helps to extract the lines to drop and remove it for the Dataframe.

C.2 Conditions justifications

Two is for observations on polynomial fits that derive for mathematics properties. The third born on the many observations that i realize after the creation of visualizer, I see the parameter of 0.001 for near lines and I put the value

Bibliography

[1] P. Eric, *Solar magnetohydrodynamics*. Kluwer, 1982.

[2] J.-M. Malherbe, "Jules janssen, the birth of solar physics, the foundation of meudon observatory and the mont blanc adventure (1875-1895)," *HAL CNRS*, Aug. 2022.

[3] S. A. Hamouda, F. F. Alfarjani, and F. Y. Elfituri, "Sunspots production and relation to other phenomena: A review," *International Journal of Science and Research Methodology*, 06 2018.

[4] F. Peter, *Solar Astrophysics*. Cambridge research and instrumentation, 1990.

[5] T. A. Nieminen, "Solar line asymmetries: Modelling the effect of granulation on the solar spectrum," *arXiv*, Aug. 2017. arXiv:1708.06408 [astro-ph].

[6] M. Ellwarth, B. Ehmann, S. Schäfer, and A. Reiners, "Convective characteristics of fe i lines across the solar disc," *Astronomy and Astrophysics*, vol. 680, p. A62, Dec. 2023.

[7] D. F. Gray and B. Oostra, "The solar-flux third granulation signature," *The Astrophysical Journal*, vol. 852, p. 42, Jan. 2018. ADS Bibcode: 2018ApJ...852...42G.

[8] D. F. Gray, "The third signature of stelar granulation," *The Astrophysical Journal*, vol. 697, p. 1032, May 2009.

[9] D. Hamilton and J. B. Lester, "A technique for the study of stellar convection: The visible solar flux spectrum," *Publications of the Astronomical Society of the Pacific*, vol. 111, p. 1132, Sept. 1999.

[10] D. Dravins, L. Lindegren, and A. Nordlund, "Solar granulation - influence of convection on spectral line asymmetries and wavelength shifts," *Astronomy and Astrophysics*, vol. 96, p. 345–364, Mar. 1981.

[11] D. F. Gray and T. Pugh, "The third signature of granulation in bright-giant and supergiant stars," *The Astronomical Journal*, vol. 143, p. 92, Mar. 2012.

[12] A. Reiners, N. Mrotzek, U. Lemke, J. Hinrichs, and K. Reinsch, "The iag solar flux atlas: Accurate wavelengths and absolute convective blueshift in standard solar spectra," *Astronomy and Astrophysics*, vol. 587, p. A65, Mar. 2016.

[13] H. H. Plaskett, "Solar granulation," *Monthly Notices of the Royal Astronomical Society*, vol. 96, p. 402, Mar. 1936. ADS Bibcode: 1936MNRAS..96..402P.

[14] B. Carroll and D. Ostlie, *An Introduction to Modern Astrophysics*. Cambridge University Press, 2017.

[15] G. Nave, S. Johansson, R. C. M. Learner, A. P. Thorne, and J. W. Brault, "A new multiplet table for fe i," *The Astrophysical Journal Supplement Series*, vol. 94, p. 221, Sept. 1994.

[16] D. F. Gray, *The Observation and Analysis of Stellar Photospheres*. Cambridge University Press, 3 ed., 2005.

[17] J. P. Boyd, *Solving Transcendental Equations: The Chebyshev Polynomial Proxy and Other Numerical Rootfinders, Perturbation Series, and Oracles*. SIAM, Oct. 2014. Google-Books-ID: ANGgBAAAQBAJ.